Bistability of travelling waves and wave-pinning states in a mass-conserved reaction-diffusion system:
From bifurcations to implications for actin waves [*]

Jack M. Hughes[†], Saar Modai[‡], Leah Edelstein-Keshet[†], and Arik Yochelis[§]

Abstract. Eukaryotic cells demonstrate a wide variety of dynamic patterns of filamentous actin (F-actin) and its regulators. Some of these patterns play important roles in cell functions, such as distinct motility modes, which motivate this study. We devise a mass-conserved reaction-diffusion model for active and inactive Rho-GTPase and F-actin in the cell cortex. The mass-conserved Rho-GTPase system promotes F-actin, which feeds back to inactivate the former. We study the model on a 1D periodic domain (edge of thin sheet-like cell) using bifurcation theory in the framework of spatial dynamics, complemented with numerical simulations. Among several discussed bifurcations, the analysis centers on the unfolding of the codimension-2 long wavelength and finite wavenumber Hopf instability, in which we describe a rich structure of steady wave-pinning states (a.k.a. mesas, obeying the Maxwell construction), propagating coherent solutions (fronts and excitable pulses), and travelling and standing waves, all distinguished by mass conservation regimes and classified by domain sizes. Specifically, we highlight the unexpected conditions for bistability between steady wave-pinning and travelling wave states on moderate domain sizes. These results uncover and exemplify possible mechanisms of coexistence, robustness, and transitions between distinct cellular motility modes, including directed migration, turning, and ruffling. More broadly, the results indicate that dissipative reaction-diffusion models comprising mass conservation have distinct pattern formation mechanisms that motivate further investigations, such as the unfolding of codimension-3 instabilities and T-points.

Key words. pattern formation, actin waves, travelling waves, wave-pinning, reaction-diffusion, mass conservation

MSC codes. 92C17, 37G15, 37M20, 37N25, 58J55

1. Introduction. In his work on morphogenesis [54], Alan Turing was concerned with spontaneous symmetry-breaking possibly leading to patterns of chemicals ("morphogens") governing cell fates in embryo development ("morphogenesis"). Since that time, exotic patterns of various proteins have even been visualized within eukaryotic cell cytoskeletons [5, 8, 9], and associated with cellular functions such as division or crawling. In the context of cell motility, patterns of proteins ("Rho-GTPases") that regulate the assembly and distribution of filamentous actin (F-actin, a biopolymer) play an important role. Rho-GTPases can spontaneously self-organize, creating "chemical prepatterns" that define the "front" (Rac) or "rear"

[†]Department of Mathematics, University of British Columbia, Vancouver, Canada (jhughes@math.ubc.ca, keshet@math.ubc.ca).

[‡]Department of Physics, Ben-Gurion University of the Negev, Be'er Sheva 8410501, Israel (modais@post.bgu.ac.il).

[§]Swiss Institute for Dryland Environmental and Energy Research, Blaustein Institutes for Desert Research, Ben-Gurion University of the Negev, Sede Boqer Campus, Midreshet Ben-Gurion 8499000, and Department of Physics, Ben-Gurion University of the Negev, Be'er Sheva 8410501, Israel (yochelis@bgu.ac.il).

(Rho) of a cell (a.k.a. cell polarization) [27]. At the front, the GTPase Rac promotes F-actin assembly, which powers the protrusion of the cell edge and can induce cell motility. These actin dynamics are important for directed migration of eukaryotic cells, such as white blood cells that move toward sites of inflammation [60, 61]. It also governs the formation of the equatorial division furrow in a dividing cell [28]. Mutations of the Rho-GTPases can also contribute to the occurrence of metastatic cancer [63].

While F-actin assembly is typically downstream of Rho-GTPases (such as Rac or Rho), in some cases, there is also evidence for negative feedback from F-actin to the GTPase (e.g. by recruiting a "GAP", an effector that causes inactivation of the GTPase). Broadly, the dual interactions between GTPases and F-actin result in a variety of "exotic" dynamic patterns collectively known as "actin waves" [3, 6, 8, 9, 12, 19, 25, 26, 37, 42, 58]. Among the experimental observations, we find rhythmic waves of F-actin and protrusion of the cell edge (Fig. 1 in [26]), lateral waves along a cell edge (Fig. 1 in [6] and space-time plots in [19]), interconversion of travelling and standing waves along a cell diameter (Fig. 1 in [62]) and waves on the cell cortex (Fig. 1 in [65]). The presence of these dynamic events appears to be ubiquitous, while the proposed underlying mechanisms vary. A rich collection of experimental, theoretical, and joint experiment-modelling literature is dedicated to exploring such phenomena [2, 7, 10, 32].

Mathematical modelling and analysis are often plausible methods to investigate pattern formation mechanisms in natural systems as well as to study hypothesized underlying interactions. However, mathematical models for the emerging "actin waves" that couple F-actin and its regulators often tend to be complex, needing to rely on numerical simulations to recapitulate experimental observations [2, 10]. The drawback, however, with studies based solely on simulations is that conclusions obtained may obscure the role of generic emergent behaviours in favour of model details [3, 4, 21]. Moreover, the parameter space of many models is typically very large, so finding biological regimes or mapping out the possible behaviours may be impractical. Even if resemblance to observations can be argued as support for such models, it can be difficult to understand, from simulations alone, how patterns emerge, interact, coexist, and affect each other's stability. Lacking such insights makes it difficult to suggest nontrivial predictions, which are essential to the validation of models. Here, we show that mechanistic understanding can be obtained via a relatively simple "toy model" that is amenable to analysis, specifically in the form of spatial dynamics. Examples, in the context of actin waves, where this approach has proven highly informative, include [9, 66].

Our aim, hence, is to identify a (simple) polynomial-type but relevant prototype model from which generic mechanisms for GTPase-actin dynamics, in the context of cell motility, can be drawn. We pose the following questions:

(Q1) Based on previous works [16, 31, 66] that show distinct regimes of patterns in parameter space, is it possible to identify a mechanism for *bistability* of travelling waves and polarization in dissipative reaction-diffusion models with mass conservation?

(Q2) What are the implications for cell motility modes? Such modes (summarized in Figure 1) include (a) steady and symmetric patterns, (b) polarized patterns, corresponding to directed migration, (c) turning or rotating cells, (d) ruffling cells, with several protrusions ("lamellipodia") circulating around their perimeter.

To address the above, we simplify a three-variable mass-conserving reaction-diffusion model by Holmes *et al.* [30], in one space dimension (1D) on a ring (periodic cell edge) and use
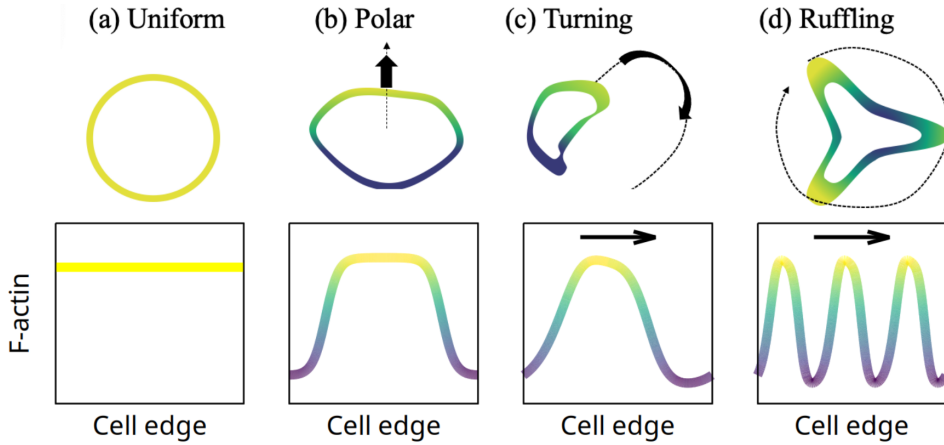
Figure 1: Schematic representation of cells and corresponding F-actin dynamics at the cell edge. Top row: four cell behaviours showing typical cell shapes and dynamics, together with F-actin distribution along the cell edge; light (dark) colour indicates high (low) F-actin concentration. Bottom row: Respective, numerical solutions on a one-dimensional (1D) domain with periodic boundary conditions. (a) Stable high uniform F-actin distribution depicting an unpolarized ("resting") cell. (b) Polar distribution associated with directed cell migration. (c) Travelling wave (TW) with a single wavelength in the periodic domain. This TW would lead the cell to crawl/turn in a circular arc. (d) Travelling wave with three wavelengths, resulting in a "ruffling" behaviour, with three protrusions circulating around its edge.

bifurcation analysis to dissect it.

The paper is organized as follows:

Section 2, modification of the dissipative mass-conserving reaction-diffusion model for actin waves by Holmes *et al.* [30];

Section 3, linear analysis of the homogeneous steady states (HSSs) in two-parameter space: we trace out the locus of distinct bifurcations and identify a codimension-2 point where a steady long wavelength and finite wavenumber Hopf instability emerge simultaneously;

Section 4, weakly nonlinear analysis of the finite wavenumber Hopf bifurcation, explaining the focus on the travelling waves (TWs);

Section 5, numerical bifurcation analysis via the continuation method to investigate the emerging structures identified in Section 3: we track excitable pulses (EPs), travelling fronts (TFs), and static "wave-pinning" (WP) solutions in large domains, as well as TWs and WP solutions in the moderately sized domain;

Section 6, numerical simulations to investigate large amplitude perturbations and the robustness of TW and WP solutions;

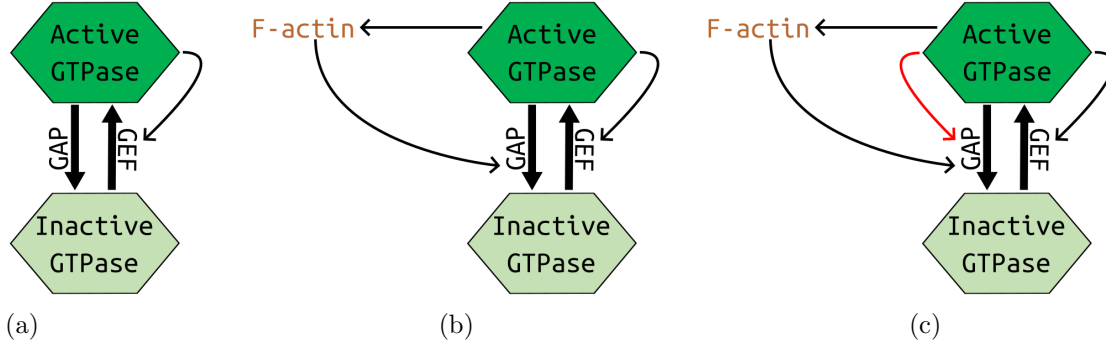**Section 7,** conclusion of the findings and outlook.

Figure 2: Schematic diagrams of several Rho-GTPase feedback-loop models. (a) The "wave-pinning" model (2.1) comprises a single GTPase with active (dark) and inactive (light) forms that are interconverted by the enzymatic action of a GEF (activation) and a GAP (inactivation). The total amount of GTPase remains constant (mass conservation) [45]. The thin arrow represents saturating positive feedback of active GTPase on its own activation. (b) The "GTPase-actin" model of Holmes (2.2) incorporates assembly of F-actin downstream of the GTPase and negative feedback from F-actin (via a GAP) [30]. (c) The modified model used throughout this study, see Equation (2.3), replaces the saturating positive feedback by a combination of polynomial positive and negative (red) feedback, otherwise preserving the structure of (2.2).

2. Model equations for the GTPase-actin system.

The starting point of our modelling is the two-component mass-conserved reaction-diffusion system for cell polarization proposed by Mori *et al.* [45], and nicknamed "wave-pinning" (WP, Figure 2a). Essential features of this system are slow-fast rates of diffusion for active (u) and inactive (v) GTPase, respectively, and nonlinear kinetic terms that admit bistability in some parameter regimes [27]. On the timescales of interest (seconds, minutes) the GTPase is neither produced nor degraded, so Mori *et al.* [45] assumed the total mass of GTPase was conserved. Therefore, the bistability differs from that of generic dissipative models, as there is a single nullcline and the flow is restricted by mass conservation. In particular, since the system can be written in a gradient form, the steady-states depend on the Maxwell construction and are non-hyperbolic [14, 17, 46]. This system produces a spatially nonuniform steady solution associated with cell polarity: a high plateau of active GTPase (corresponding to the leading edge of a cell) separated by an interface from a low active GTPase plateau. Note that WP solutions are also known as "mesa" states in the context of porous media [23] and chemical patterning [36]. Holmes *et al.* [30] extended the WP system to capture "actin waves" in reasoning that is similar to the idea behind the classic FitzHugh-Nagumo (FHN) system [24, 47], where a bistable system is coupled to slow negative feedback: the (u, v)-system acts as the "bistable" part, and slow negative feedback is provided by F-actin (F), whose role is similar to a "refractory variable" in the FHN model (Figure 2b). The experiments of Michaud *et al.* [41] describe a real cell system with interactions as in the Holmes *et al.* model (although the authors chose to rederive

their own, rather similar, model system): the GTPase is Rho, it self-activates (via the GEF Ect2), and F-actin recruits a GAP (RGA-3/4) that inactivates Rho. In what follows, we simplify the original WP and actin waves model to produce the model that we will analyze in the remainder of this study.

The wave-pinning model by Mori *et al.* [45] reads in its dimensionless form as:

$$(2.1a) \qquad \frac{\partial u}{\partial t} = \left(b + \gamma \frac{u^n}{1+u^n} \right) v - Iu + D\frac{\partial^2 u}{\partial x^2},$$

$$(2.1b) \qquad \frac{\partial v}{\partial t} = -\left(b + \gamma \frac{u^n}{1+u^n} \right) v + Iu + \frac{\partial^2 v}{\partial x^2}.$$

The model conserves mass,

$$(2.1c) \qquad M := \frac{1}{L} \int_0^L [u(x,t) + v(x,t)]\, \mathrm{d}x = \text{constant},$$

where L is the domain length. Here u, v are, respectively, the levels of active and inactive Rho-GTPase, b is a basal rate of activation, I is an inactivation rate, γ is the rate of autoactivation (positive feedback of active GTPase to its own activation rate via a GEF), and $D < 1$ is the slow rate of diffusion of active GTPase relative to the inactive GTPase. (The disparity in diffusion rates stems from the fact that the active GTPase is bound to the membrane of the cell, a more viscous environment than the cytosol where the inactive GTPase resides.) This model arbitrarily assumes positive feedback onto the GEFs, but it was also shown that negative feedback onto the GAPs leads to qualitatively similar results [33]. For $n = 2$ and $I = 1$ in (2.1), WP solutions are observed over a wide range of parameters. These solutions are interpreted as polarized patterns of active GTPase [45, 46] associated with cell polarity. It is then understood that if u is the level of active Rac or Cdc42 (both Rho-GTPases that promote branched F-actin), then wherever u is high, there would locally be assembly of F-actin that can exert protrusive force on the cell membrane. Alternatively, if u represents the GTPase Rho, then there could be either F-actin assembly (by formins, proteins that nucleate F-actin strands) or local myosin activation that leads to edge contraction [50].

Holmes *et al.* [30] coupled the WP model to F-actin (F) via slow negative feedback, assuming that F increases the rate of inactivation of the GTPase u (see Figure 2b). The dynamics of F are taken to be linear and its rate of diffusion, which is very low was neglected:

$$(2.2a) \qquad \frac{\partial u}{\partial t} = \left(b + \gamma \frac{u^2}{1+u^2} \right) v - \left(1 + s\frac{F}{1+F} \right) u + D\triangle u,$$

$$(2.2b) \qquad \frac{\partial v}{\partial t} = -\left(b + \gamma \frac{u^2}{1+u^2} \right) v + \left(1 + s\frac{F}{1+F} \right) u + \triangle v,$$

$$(2.2c) \qquad \frac{\partial F}{\partial t} = \theta(pu - F).$$

We note that conceptually, system (2.2) is similar to the actin waves model of [66]. We later draw comparisons for selected values of the total GTPase concentration M.

Table 1: Parameter descriptions and values used throughout this study.

Parameter	Definition	Value
b	GTPase basal activation rate	[0,4.5]
γ	GTPase autocatalytic activation rate	3.557
s	Strength of F-actin negative feedback	[0,13]
θ	F-actin time scale parameter	0.6
p_0	F-actin basal assembly rate	0.8
p_1	GTPase-dependent F-actin assembly rate	3.8
D	Active GTPase rate of diffusion	0.1
D_F	F-actin rate of diffusion	0.001
M	Average total GTPase concentration	2,4.5

System (2.2) is relatively cumbersome since it comprises several rational ("Hill") functions. Hence, we choose to simplify it with polynomial dependencies while maintaining the mass-conserved property of the (u,v)-subsystem, the positive feedback of u on the assembly of F (taking $p_1 \geq 0$), and the slow negative feedback of F on u (see Figure 2c):

$$(2.3a) \qquad \frac{\partial u}{\partial t} = (b + \gamma u^2)v - (1 + sF + u^2)u + D\frac{\partial^2 u}{\partial x^2},$$

$$(2.3b) \qquad \frac{\partial v}{\partial t} = -(b + \gamma u^2)v + (1 + sF + u^2)u + \frac{\partial^2 v}{\partial x^2},$$

$$(2.3c) \qquad \frac{\partial F}{\partial t} = \theta(p_0 + p_1 u - F) + D_F\frac{\partial^2 F}{\partial x^2}.$$

In what follows, we analyze system (2.3) on a 1D domain with either periodic or Neumann boundary conditions (PBCs or NBCs, respectively), interpreted as a ring corresponding to the cell perimeter (see Figure 1), or a cell diameter, respectively,

$$(2.4) \qquad Q(0,t) = Q(L,t) \qquad \text{and} \qquad \partial_x Q(0,t) = \partial_x Q(L,t) = 0,$$

where $Q(x,t) := (u,v,F)^T$ and the superscript T stands for transpose.

For analysis purposes, we use the strength of F-actin negative feedback, s, as the primary bifurcation parameter and the GTPase basal activation rate b as the secondary parameter. See also the complete list of parameter values and their biological meanings in Table 1.

3. Linear analysis of homogeneous steady states (HSSs). The HSSs of (2.3) (after setting $\partial_t = \partial_x = 0$) are solutions to

$$(3.1a) \qquad 0 = (b + \gamma u^2)v - (1 + sF + u^2)u,$$

$$(3.1b) \qquad 0 = \theta(p_0 + p_1 u - F),$$

$$(3.1c) \qquad 0 = u + v - M.$$

The third equation comes from mass conservation. Elimination of v and F, $v = M - u$ and $F = p_0 + p_1 u$, leads to

$$(3.2) \qquad \nu(u) \equiv (b + \gamma u^2)(M - u) - (1 + s(p_0 + p_1 u) + u^2)u = 0.$$

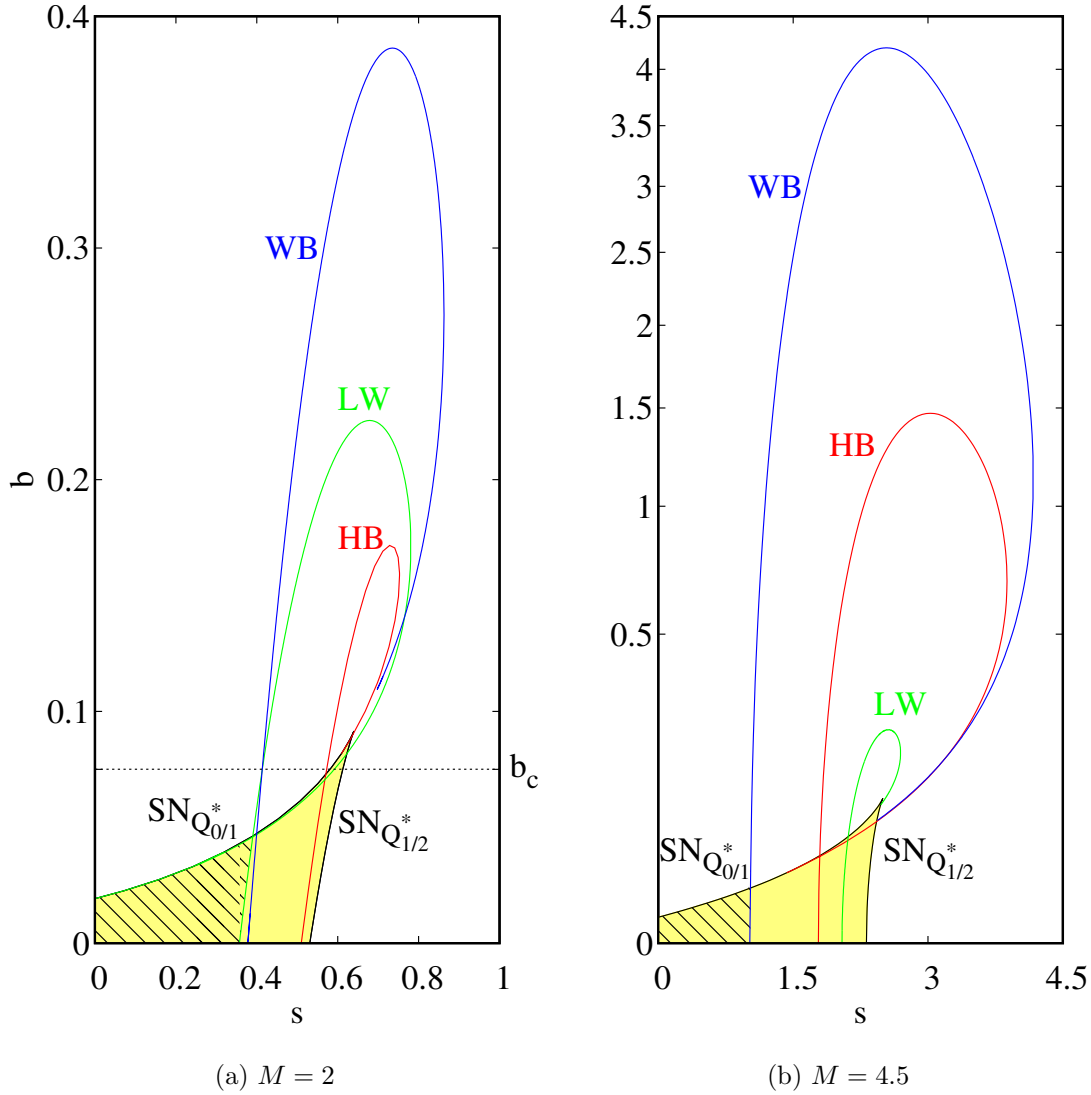(a) $M = 2$ (b) $M = 4.5$

Figure 3: The linear onsets of bifurcations along homogeneous steady states are shown as curves in the (s, b) parameter plane, where s is the strength of F-actin negative feedback and b is the GTPase basal activation rate. The bifurcation onsets are computed using (3.3), where LW - long wavelength (green), WB - finite wavenumber Hopf (blue), HB - homogeneous Hopf (red). (a) Low vs (b) high total GTPase concentration (M) differ since in (a) LW occurs before HB while in (b) it is reversed (note that in (b) we use a logarithmic dependence of b). The solid yellow-shaded region indicates the coexistence of three HSSs ($Q^*_{0,1,2}$) with at most one stable, where SN indicates saddle-nodes of respective HSSs, ending at a cusp bifurcation slightly below $b = 0.1$. The cross-hatched region indicates bistability of the HSSs. The horizontal dotted line in (a) at $b := b_c \approx 0.067$, corresponds to a one-parameter slice shown in Figure 4, where a codimension-2 LW/WB instability occurs. Other parameter values as in Table 1.
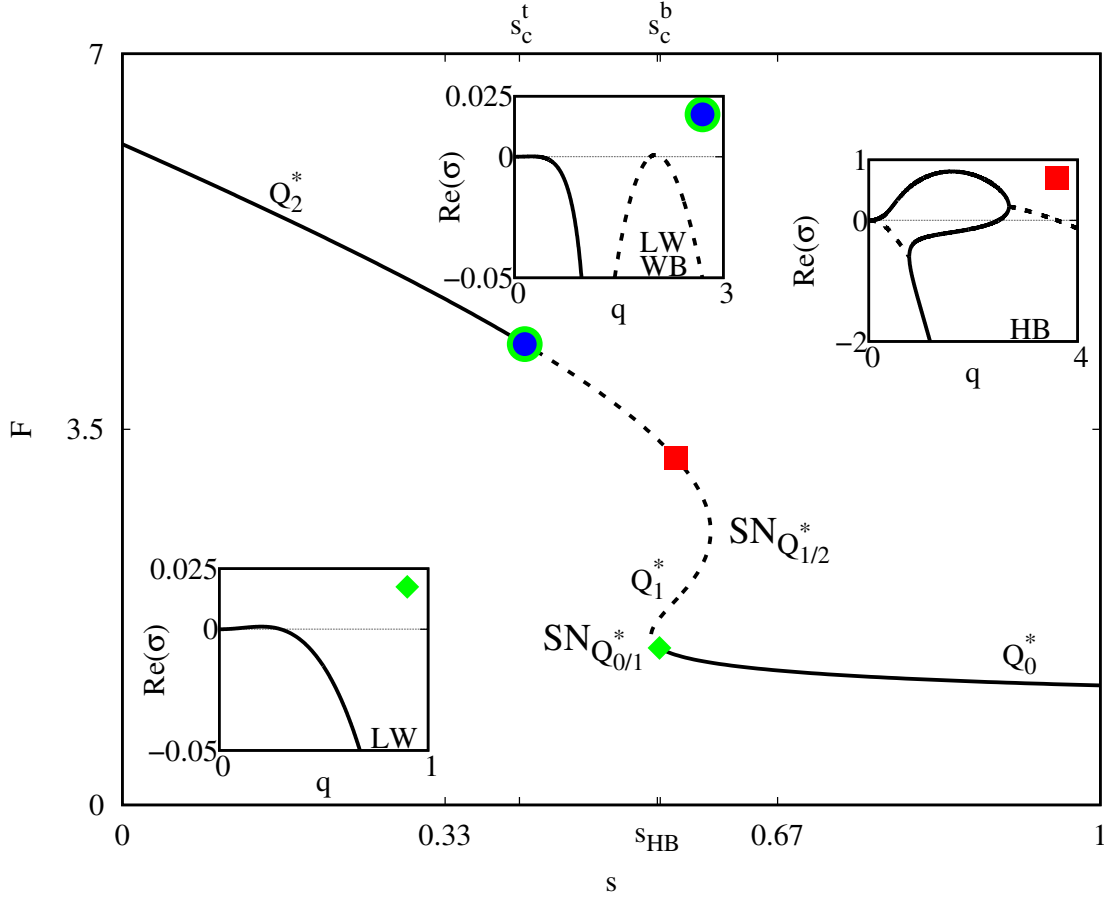
Figure 4: One-parameter bifurcation diagram for the F-actin component as a function of GTPase inactivation rate s, along the dotted line slice in Figure 3a, where $Q^*_{0,1,2}$ are homogeneous steady states; solid (dashed) lines denote linear stability (instability). The values $(s^t_c, s^b_c, s_{HB}) \approx (0.406, 0.550, 0.565)$ denote the top codimension-2 long wavelength (LW)/finite wavenumber Hopf (WB) instability onset about Q^*_2, LW instability onset about Q^*_0, and the homogeneous Hopf (HB) bifurcation, respectively. Insets show dispersion relations at bifurcation onsets indicated by corresponding shapes (circle, square, etc.); the growth rate $\mathrm{Re}(\sigma(q))$ of perturbations with wavenumber q is a solid (dashed) line for real (complex conjugate) parts. Parameter values as in Table 1 with $M = 2$ and $b = b_c \approx 0.067$.

At least one biologically relevant HSS $Q^* = (u^*, v^*, F^*)^T$ (i.e. $u^*, v^*, F^* > 0$) exists for $b, \gamma, s, p_0, p_1, M > 0$ by the *Intermediate Value Theorem* after noting that

$$\nu(0) = bM > 0,$$
$$\nu(M) = -(1 + s(p_0 + p_1 M) + M^2)M < 0.$$

Note that $b > 0$ excludes the existence of trivial HSSs. In Figure 3, we show the regions where these solutions coexist, i.e., $Q^*_{0,1,2}$, where the yellow shaded region corresponds to the existence of multiple steady states and is limited by two folds (black lines) that emanate from a cusp bifurcation. The cross-hatched yellow region denotes bistability of HSSs.

Next, we perform a linear stability analysis of infinitesimal perturbations in the infinite domain by expanding

$$Q = Q^* + \epsilon Q_1 + \mathcal{O}(\epsilon^2),$$

where $|\epsilon| \ll 1$ and Q_1 is of $\mathcal{O}(1)$. The function Q_1 is given by

$$Q_1 = \begin{pmatrix} u_1 \\ v_1 \\ F_1 \end{pmatrix} e^{\sigma t + iqx} + c.c.,$$

where σ is the growth rate of the wavenumber q, and $c.c.$ stands for complex conjugate. Consequently, linearization leads to

$$(3.3) \qquad \sigma \begin{pmatrix} u_1 \\ v_1 \\ F_1 \end{pmatrix} = \mathcal{L}(Q^*) \begin{pmatrix} u_1 \\ v_1 \\ F_1 \end{pmatrix},$$

where $\mathcal{L}$ is the Jacobian of (2.3)

$$(3.4) \qquad \mathcal{L} = \begin{pmatrix} 2\gamma u^* v^* - 1 - F^* s - 3u^{*2} - Dq^2 & b + \gamma u^{*2} & -su^* \\ 1 + F^* s + 3u^{*2} - 2\gamma u^* v^* & -b - \gamma u^{*2} - q^2 & su^* \\ \theta p_1 & 0 & -\theta - D_F q^2 \end{pmatrix}.$$

By solving $\det(\mathcal{L} - \sigma \mathbb{I}) = 0$ for $\sigma(q)$, we obtain three dispersion relations from which instability onsets are classified [18]. Due to mass conservation, for $q = 0$, we expect a persistent zero eigenvalue since $\mathcal{L}(Q^*)$ is singular. Linear stability of Q^* is, therefore, determined if all growth rates $\sigma(q)$ have negative real parts $\forall q \geq 0$, whereas the instability onsets occur once $\mathrm{Re}(\sigma(q_c)) = 0$ for some $q_c \geq 0$. If additionally, $\mathrm{Im}(\sigma(q_c)) = \omega_c \neq 0$, then the instability is of oscillatory type so that two dispersion curves are complex conjugates.

In our setting, we are mainly interested in two instabilities: the steady long wavelength (LW) and the finite wavenumber Hopf (WB). The LW occurs as in gradient systems, i.e., this instability occurs when the concavity of $\max_\sigma \mathrm{Re}(\sigma(q))$ changes sign at $q = 0$ [18], since at least one $\sigma(0) = 0$ by mass conservation. The WB is an oscillatory type, simultaneously giving rise to both travelling waves (TW) and standing waves (SWs) [34]. In addition, we find it informative to monitor bifurcations occurring when the HSS is linearly unstable, i.e., not only the LW and the WB but also the homogenous Hopf (HB). Consequently, we show in Figure 3, selected two-parameter diagrams while varying (s, b), for $M = 2$ and $M = 4.5$, in which we identify saddle-nodes (SNs) of HSS (black) and the locus of bifurcation onsets: HB (red), WB (blue), and LW (green). For an illustration of the bifurcation onsets and the following analysis, we focus on a selected slice at $b = b_c \approx 0.067$ (dotted line in Figure 3a) exhibiting a codimension-2 point of LW/WB instabilities for $M = 2$, as shown in Figure 4. We focus on $M = 2$ since for $M = 4.5$, the LW loop is the most inner one (see Figure 3b),

excluding the occurrence of the LW/WB instability. Nevertheless, we briefly demonstrate the similarities and differences to the case of $M = 4.5$ (in Section 5) and compare with the results obtained by Yochelis *et al.* [66], see also Appendix B. We note that for $b \approx 0.14$, in a region above the cusp bifurcation of HSSs (shaded yellow), there is another codimension-2 LW/WB bifurcation. The latter is outside the scope of this work and will be addressed elsewhere.

4. Weakly nonlinear analysis of oscillatory solutions. We proceed here with the analysis of oscillatory solutions bifurcating from LW/WB, $s = s_c^t \approx 0.406$ and $b = b_c \approx 0.067$, see Figure 4. The solutions that bifurcate from the long wavelength onset are stationary and in a subcritical direction (see Figure 8), namely toward the linearly stable regime. The travelling (TW$_\lambda$) and standing (SW$_\lambda$) waves with critical wavelength $\lambda = 2\pi/q_c \approx 3.093$ that emerge from the finite wavenumber Hopf bifurcation are in the supercritical direction with $\omega_c \approx 0.388$. To identify both the stability and criticality of pure TWs and SWs, we perform weakly nonlinear stability analysis, a.k.a. multiple timescales or amplitude equation methods. From reflection symmetry ($x \to -x$), we expect the approximate solution to be a combination of right- and left-travelling (counter-propagating) modes:

$$(4.1) \qquad Q \sim \boldsymbol{B}_L(\tau) e^{i(\omega_c t + q_c x)} + \boldsymbol{B}_R(\tau) e^{i(\omega_c t - q_c x)} + c.c.$$

Here $\boldsymbol{B}_L, \boldsymbol{B}_R$ are complex, slowly varying amplitudes that depend on the slow temporal variable τ (as compared to the fast time t).

4.1. Small parameter expansion. Let ϵ be a small parameter such that $\epsilon^2 \propto |s - s_c^t| \ll 1$ is a measure of the system's distance from the onset of instability. Then $s = s_c^t + \epsilon^2 \widetilde{s}$, where $\widetilde{s}$ is of $\mathcal{O}(1)$. We set the power of ϵ in the slow temporal scale by observing the dependence of the growth rate σ on ϵ. Finding a quadratic dependence, $\sigma \propto \epsilon^2$, we arrive at the temporal scaling $\tau = \epsilon^2 t$. The scaling for the slowly varying amplitudes is therefore set to $\widetilde{\boldsymbol{B}}_L = \epsilon \boldsymbol{B}_L$, $\widetilde{\boldsymbol{B}}_R = \epsilon \boldsymbol{B}_R$. This scaling is typical for such derivations. Next, we expand Q in powers of ϵ:

$$(4.2a) \qquad u = u^* + \epsilon u_1(x, t, \tau) + \epsilon^2 u_2(x, t) + \epsilon^3 u_3(x, t) + \cdots,$$

$$(4.2b) \qquad v = v^* + \epsilon v_1(x, t, \tau) + \epsilon^2 v_2(x, t) + \epsilon^3 v_3(x, t) + \cdots,$$

$$(4.2c) \qquad F = F^* + \epsilon F_1(x, t, \tau) + \epsilon^2 F_2(x, t) + \epsilon^3 F_3(x, t) + \cdots,$$

where:

$$(4.3a) \qquad u_1 = B_{Lu}(\tau) e^{i(\omega_c t + q_c x)} + B_{Ru}(\tau) e^{i(\omega_c t - q_c x)} + c.c.,$$

$$(4.3b) \qquad v_1 = B_{Lv}(\tau) e^{i(\omega_c t + q_c x)} + B_{Rv}(\tau) e^{i(\omega_c t - q_c x)} + c.c.,$$

$$(4.3c) \qquad F_1 = B_{LF}(\tau) e^{i(\omega_c t + q_c x)} + B_{RF}(\tau) e^{i(\omega_c t - q_c x)} + c.c.,$$

i.e. replacing $Q \to Q_1$ in (4.1), with ω_c, q_c denoting the critical frequency and wavenumber at the instability onset. Substitution of (4.3) and all the scaling terms into (2.3) and separating into powers of ϵ (up to third order), yields at each order ϵ^i the corresponding equation:

$$(4.4) \qquad \widetilde{\mathcal{L}} Q_i = \boldsymbol{R}_i,$$

where $\widetilde{\mathcal{L}} := i\omega_c \mathbb{I} - \mathcal{L}|_{s=s_c^t}$, $\mathbb{I}$ is the identity matrix, and $\boldsymbol{R}_i$ includes nonlinear terms and depends on lower order contributions to the solution that are already known (meaning on $Q_1, ..., Q_{i-1}$).

At leading order, we recover the steady state Q^* at $s = s_c^t$, whereas order ϵ yields

$$\widetilde{\mathcal{L}}Q_1 = \boldsymbol{R}_1 = 0. \tag{4.5}$$

Solution of (4.5) gives the so-called eigen-relations between the TW amplitudes:

$$B_{Lu} = \frac{D_F q^2 + \theta + i\omega_c}{p_1 \theta} B_{LF} := b_u B_{LF}, \tag{4.6a}$$

$$B_{Lv} = \frac{s_c^t u_c^*}{b + \gamma u_c^{*2}} B_{LF}$$
$$+ \frac{1 + D_u q^2 + (p_0 + p_1 u_c^*) s_c^t + (3 + 2\gamma) u_c^{*2} - 2\gamma M u_c^* + i\omega_c}{b + \gamma u_c^{*2}} b_u B_{LF} := b_v B_{LF}, \tag{4.6b}$$

where $(u_c^*, v_c^*, F_c^*) = (u^*, v^*, F^*)|_{s=s_c^t}$. Similarly, proceeding to the higher orders, we obtain:

$$\boldsymbol{R}_2 = \left\{ \left[(\gamma M - (3 + \gamma) u_c^*) u_1 + 2u_c^* \gamma v_1 - s_c^t F_1 \right] u_1 - p_0 \widetilde{s} u_c^* - p_1 \widetilde{s} u_c^{*2} \right\} \begin{pmatrix} 1 \\ -1 \\ 0 \end{pmatrix}, \tag{4.7}$$

$$\boldsymbol{R}_3 = -\frac{\partial}{\partial \tau} \begin{bmatrix} u_1(\tau) \\ v_1(\tau) \\ F_1(\tau) \end{bmatrix} + \left\{ \left[(2\gamma M - 6u_c^*) u_1 + 2u_c^* \gamma (v_1 - u_1) - F_1 s_c^t \right] u_2 \right\} \begin{pmatrix} 1 \\ -1 \\ 0 \end{pmatrix} \tag{4.8}$$
$$+ \left\{ \left[2\gamma u_c^* v_2 - s_c^t F_2 + (p_1 u_c^* - p_0) \widetilde{s} \right] u_1 + (\gamma v_1 - u_1) u_1{}^2 - \widetilde{s} u_c^* F_1 \right\} \begin{pmatrix} 1 \\ -1 \\ 0 \end{pmatrix}.$$

4.2. Solvability condition and amplitude equations. In some cases, $\boldsymbol{R}_i$ contains resonant terms with respect to the critical frequency. Such resonant terms can cause the approximate solution (4.1) to diverge, contradicting the assumption that higher order terms in (4.2) contribute smaller and smaller corrections (given the smallness of ϵ). In that case, the solution is only valid for a very short period of time and tiny deviation from the onset of instability. To avoid such terms, we use the *Fredholm alternative* as a formal framework for applying the solvability condition by utilizing an inner product:

$$\langle f, g \rangle \equiv \iint_{T, \lambda} \bar{f} g \, \mathrm{d}x \mathrm{d}t, \tag{4.9}$$

where $T = 2\pi/\omega_c$ and $\lambda = 2\pi/q_c$. This leads to a solvability condition

$$\langle \boldsymbol{N}, \boldsymbol{R}_i \rangle = \langle \boldsymbol{N}, \widetilde{\mathcal{L}} \boldsymbol{S}_i \rangle = \langle \widetilde{\mathcal{L}}^\dagger \boldsymbol{N}, \boldsymbol{S}_i \rangle = 0, \tag{4.10}$$

where $\widetilde{\mathcal{L}}^\dagger$ is the adjoint of $\widetilde{\mathcal{L}}$ and the components of the nullvector

$$\boldsymbol{N} = \begin{pmatrix} N_1 \\ N_2 \\ N_3 \end{pmatrix} e^{-i(i\omega_c \mp qx)}$$

are related by

$$(4.11a) \qquad N_1 = -\frac{\left(b + q^2 + \gamma u_c^{*2} + i\omega_c\right)\left(D_F q^2 + \theta + i\omega_c\right)}{s_c^t u_c^* \left(q^2 + i\omega_c\right)} N_3,$$

$$(4.11b) \qquad N_2 = -\frac{\left(b + \gamma u_c^{*2}\right)\left(D_F q^2 + \theta + i\omega_c\right)}{s_c^t u_c^* \left(q^2 + i\omega_c\right)} N_3.$$

Applying the solvability condition, we obtain

$$Q_2 = \left\{ \begin{pmatrix} a_1 \\ a_2 \\ a_3 \end{pmatrix} e^{2i\omega_c t + 2iq_c x} + \begin{pmatrix} b_1 \\ b_2 \\ b_3 \end{pmatrix} e^{2i\omega_c t - 2iq_c x} + \begin{pmatrix} c_1 \\ c_2 \\ c_3 \end{pmatrix} e^{2i\omega_c t} + \begin{pmatrix} d_1 \\ d_2 \\ d_3 \end{pmatrix} e^{2iq_c x} + c.c \right\}$$

$$+ \begin{pmatrix} h_1 \\ h_2 \\ h_3 \end{pmatrix} + E \begin{pmatrix} u_1 \\ v_1 \\ F_1 \end{pmatrix},$$

where E is a constant, which, for simplicity, we set to zero. All other coefficients are obtained numerically using *Mathematica*.

Finally, inserting Q_2 into the form of $\boldsymbol{R}_3$, and expanding in powers of $e^{i(\pm\omega_c t \pm q_c x)}$, yields after applying (4.10) and rescaling back to original variables, the amplitude equations:

$$(4.12a) \qquad \dot{B}_{LF} = \alpha(s - s_c^t)B_{LF} - \left[\gamma|B_{LF}|^2 + \eta|B_{RF}|^2\right]B_{LF},$$

$$(4.12b) \qquad \dot{B}_{RF} = \alpha(s - s_c^t)B_{RF} - \left[\gamma|B_{RF}|^2 + \eta|B_{LF}|^2\right]B_{RF}.$$

The coefficients obtained numerically using *Mathematica* are found to be $\alpha = 2.1507 - 1.6028i$, $\gamma = 0.05798 + 0.0150i$, $\eta = 0.0624 + 0.1607i$.

4.3. Validation. To validate the amplitude equations (4.12), we use polar forms $B = \rho \exp i\Phi$ with the subscripts r/i denoting the real/imaginary parts of coefficients, and for convenience, rewrite in a canonic form [34]

$$(4.13a) \qquad \dot{\rho}_L = \rho_L \left[\widetilde{\alpha}_r\left(s - s_c^t\right) + \widetilde{a}_r\rho_R^2 + \widetilde{b}_r\left(\rho_L^2 + \rho_R^2\right)\right],$$

$$(4.13b) \qquad \dot{\rho}_R = \rho_R \left[\widetilde{\alpha}_r\left(s - s_c^t\right) + \widetilde{a}_r\rho_L^2 + \widetilde{b}_r\left(\rho_L^2 + \rho_R^2\right)\right],$$

$$(4.13c) \qquad \dot{\Phi}_L = \widetilde{\alpha}_i\left(s - s_c^t\right) + \widetilde{a}_i\rho_R^2 + \widetilde{b}_i\left(\rho_L^2 + \rho_R^2\right),$$

$$(4.13d) \qquad \dot{\Phi}_R = -\widetilde{\alpha}_i\left(s - s_c^t\right) - \widetilde{a}_i\rho_L^2 - \widetilde{b}_i\left(\rho_L^2 + \rho_R^2\right).$$

where $\widetilde{a}_r = \gamma_r - \eta_r \approx -0.0044$, $\widetilde{b}_r = -\gamma_r \approx -0.0624$, $\widetilde{a}_i = \gamma_i - \eta_i \approx -0.1457$, and $\widetilde{b}_i = -\gamma_i \approx -0.1607$. Steady solutions to (4.13) are

$$(4.14a) \qquad \rho = \sqrt{\frac{\widetilde{\alpha}_r}{\widetilde{b}_r}\left(s_c^t - s\right)}, \quad \text{for TWs with } (\rho_L, 0) = (\rho, 0),$$

$$(4.14b) \qquad \rho = \sqrt{\frac{\widetilde{\alpha}_r}{\widetilde{a}_r + 2\widetilde{b}_r}\left(s_c^t - s\right)}, \quad \text{for SWs with } (\rho_L, \rho_R) = (\rho, \rho),$$
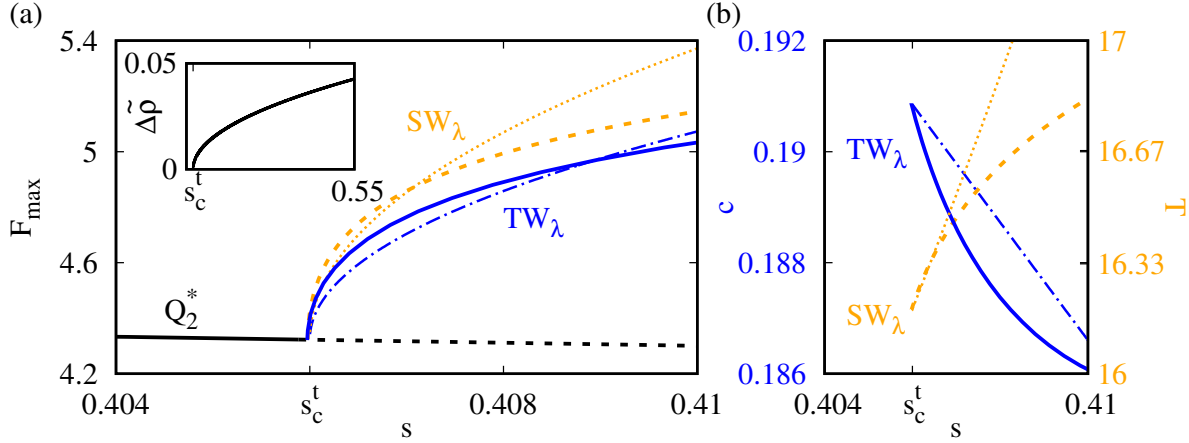
Figure 5: (a) Bifurcating branches of the primary travelling and standing waves (with wavelength $\lambda \approx 3.09$) obtained at the codimension-2 onset at $s = s_c^t \approx 0.406$ (see the slice in Figure 3a, $b = b_c \approx 0.067$), hereafter TW_λ and SW_λ, respectively. The solutions are projected onto the maximum F-actin concentration, F_{max}. We compare results from the amplitude equations (4.15) and (4.16) to numerical continuation, over spatial wavelength λ and, in the case of SW, also over the temporal period T (also obtained at the onset): Linearly stable TWs (from continuation: solid blue; from amplitude equations: dashed-dotted blue) and linearly unstable SWs (from continuation: dashed orange; from amplitude equations: dotted orange). The inset shows the difference between the total amplitudes of the TWs and SWs according to (4.16) ($\Delta\widetilde{\rho} = \widetilde{\rho}_{TW} - \widetilde{\rho}_{SW}$), indicating that TWs are larger than SWs. (b) Same as (a) but with TWs being projected onto the phase wave speed c (left vertical axis) and SWs onto the time-period T (right vertical axis), see (4.19). Other parameters as in Table 1.

and thus, the maximal values of F for TWs and SWs, respectively, are

$$(4.15) \qquad F_{max} = F^* + \begin{cases} 2\rho, & \text{for TWs;} \\ 4\rho, & \text{for SWs.} \end{cases}$$

A comparison of the TWs and SWs amplitudes vs. numerical continuation is shown in Figure 5a. See Section 5 for brief details of the numerical continuation methods. For consistency, we also replot in the inset of Figure 5, the difference in total amplitudes

$$(4.16) \qquad \widetilde{\rho} = \sqrt{\rho_L^2 + \rho_R^2} = \begin{cases} \sqrt{\dfrac{\widetilde{\alpha}_r}{\widetilde{b}_r}(s_c^t - s)}, & \text{for TWs;} \\[4mm] \sqrt{\dfrac{2\widetilde{\alpha}_r}{\widetilde{a}_r + 2\widetilde{b}_r}(s_c^t - s)}, & \text{for SWs,} \end{cases}$$

of the TWs and SWs (as opposed to plotting in terms of F_{max}) to show that the TW branch in terms of $\Delta\widetilde{\rho} = \widetilde{\rho}_{TW} - \widetilde{\rho}_{SW} > 0$, is indeed larger than the branch of SWs, as expected by a

standard theory [34]. This also agrees with the linear stability of TWs. For completeness, we also compute the frequency correction

$$(4.17) \qquad \Omega_{TW} = \left(\widetilde{\alpha}_i - \widetilde{\alpha}_r \frac{\widetilde{b}_i}{\widetilde{b}_r} \right) \left(s - s_c^t \right),$$

$$(4.18) \qquad \Omega_{SW} = \left(\widetilde{\alpha}_i - \widetilde{\alpha}_r \frac{\widetilde{a}_i + 2\widetilde{b}_i}{\widetilde{a}_r + 2\widetilde{b}_r} \right) \left(s - s_c^t \right),$$

and the modified speed and temporal period

$$(4.19) \qquad c_{TW} = \frac{\omega_c + \Omega_{TW}}{q_c}, \quad T_{SW} = \frac{2\pi}{\omega_c + \Omega_{SW}}.$$

Figure 5b compares the speed of TWs and temporal period for SWs from (4.19) with those obtained via numerical continuation.

Conducting similar computations for the left side of the LW loop, we find that the criticalities of TW and SW persist. However, above the codimension-2 point, i.e., $b > b_c \approx 0.067$, both TW and SW are initially unstable since there, WB lies inside the LW loop (i.e. linearly unstable regime of Q_2^*). Nevertheless, TWs of critical period or otherwise may still gain stability through other mechanisms far from the onset. Some of these will be demonstrated in the following section.

5. Solutions and bifurcations in the nonlinear regime. Linear stability analysis reflects the spatial separation of scales associated with the primary long wavelength (LW) and finite wavenumber Hopf (WB) instabilities. Therefore, in what follows, we find it useful to separate the analysis and investigate solutions in large domains ($L \gg \lambda$) and in moderate domains ($L \sim \mathcal{O}(m\lambda)$) along the slice depicted in Figure 4, where λ is the critical wavelength of the WB in the codimension-2 LW/WB bifurcation at $(s, b) = (s_c^t, b_c)$ and m is some small positive integer. The analysis is performed using a numerical continuation package AUTO [20]. For presentation purposes, we plot the bifurcation diagrams with a combination of the standard Sobolev H^1 norm

$$(5.1) \qquad \|Q\| := \sqrt{\frac{1}{L} \int_0^L [Q^T Q + Q'^T Q'] \, d\xi},$$

and/or with the maximum value of F over the domain, and/or the propagation speed c, where primes denote differentiation with respect to the argument. All the numerical computations involve steady-state solutions since the TWs are computed in a co-moving frame, $\xi = x - ct$. Note that since the solutions of interest obey left-right translational symmetry, we only plot branches for speed $c > 0$. For details on the implementation in AUTO, on linear stability computation, and on the direct PDE numerical integration methods, we refer the reader to Appendix A.

5.1. Coherent solutions in large domains, $L \gg \mathcal{O}(\lambda)$**.** The linear stability analysis of Q_2^* with $M = 2$ showed that the instability onset at $s = s_c^t$ is the codimension-2 LW/WB bifurcation (see Figure 4) while the homogeneous Hopf bifurcation (HB) occurs for $s > s_c^t$. This
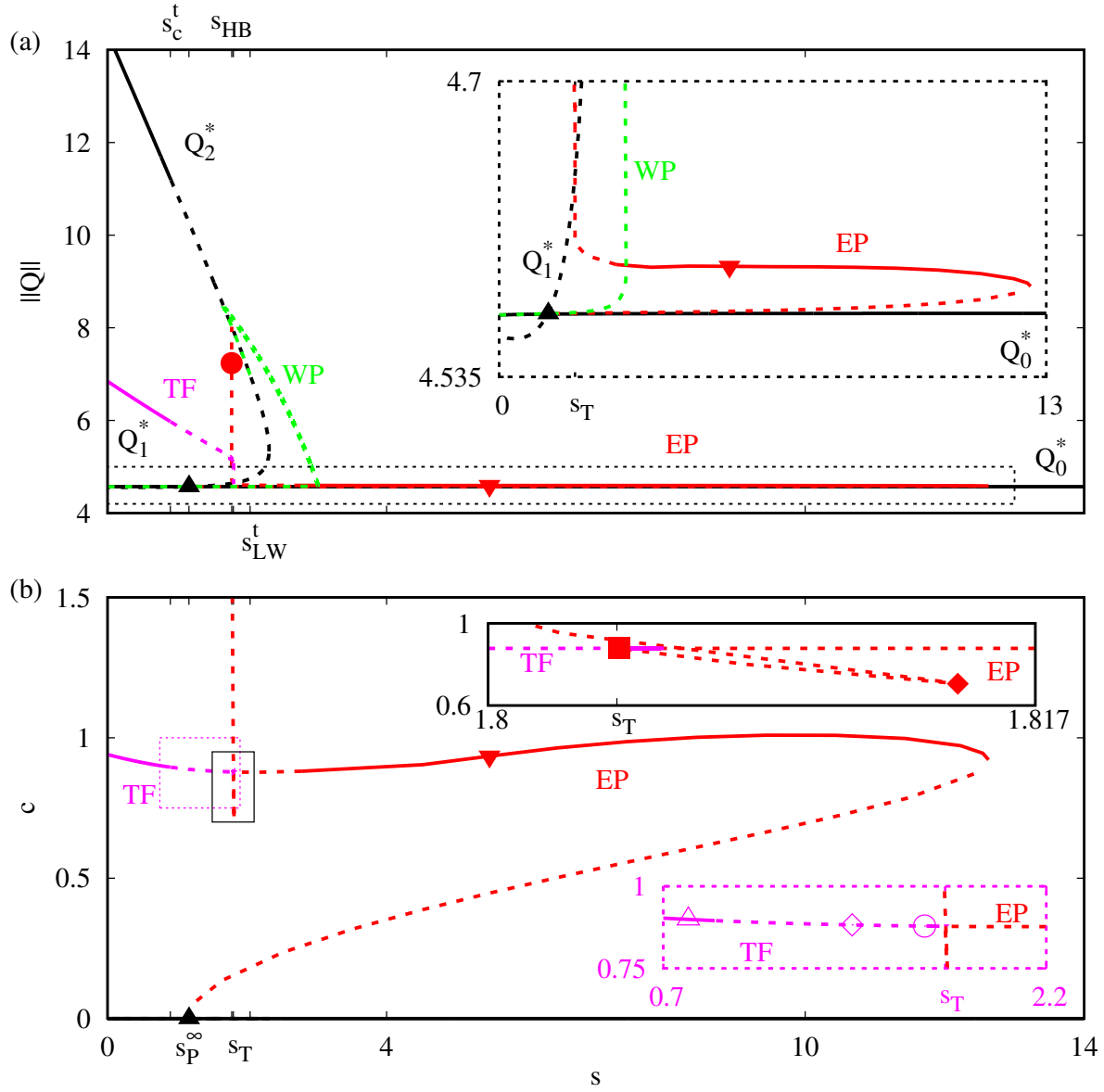
Figure 6: Bifurcation diagrams computed via numerical continuation as a function of s, showing excitable pulses (EPs), travelling fronts (TFs), wave-pinning (WP) solutions, and the homogeneous steady states $Q_{0,1,2}^*$ for $M = 4.5$ and $L = 1000 \gg \lambda \approx 1.93$ (where λ is the wavelength leading to instability of Q_2^*). The solution branches are projected with the Sobolev norm (5.1) in (a) and the propagation speed c in (b); solid (dashed) lines denote linearly stable (unstable) solutions. The inset in (a) zooms into the stable region of EPs while the insets in (b) zoom into the T-point regime that connects the EP and TF branches upon periodic and Neumann boundary conditions, respectively. The critical values $(s_c^t, s_P^\infty, s_{HB}, s_T, s_{LW}^t) = (0.908, 1.167, 1.781, 1.804, 2.044)$ represent the finite wavenumber Hopf (WB) instability of Q_2^*, the parity-breaking bifurcation (black triangle) of WP solutions to EPs, the homogeneous Hopf (HB) bifurcation onset, the T-point (red square), and the top (Q_2^*) long wavelength (LW) bifurcation, respectively. The EP branch tends to a wave speed of $c \approx 410$ at $s = s_{HB}$ but is cropped in (b). The symbols (circle, diamond, etc.) represent selected locations of solution profiles given in Figure 7. Other parameter values as in Table 1 with $b = 0.00067$.
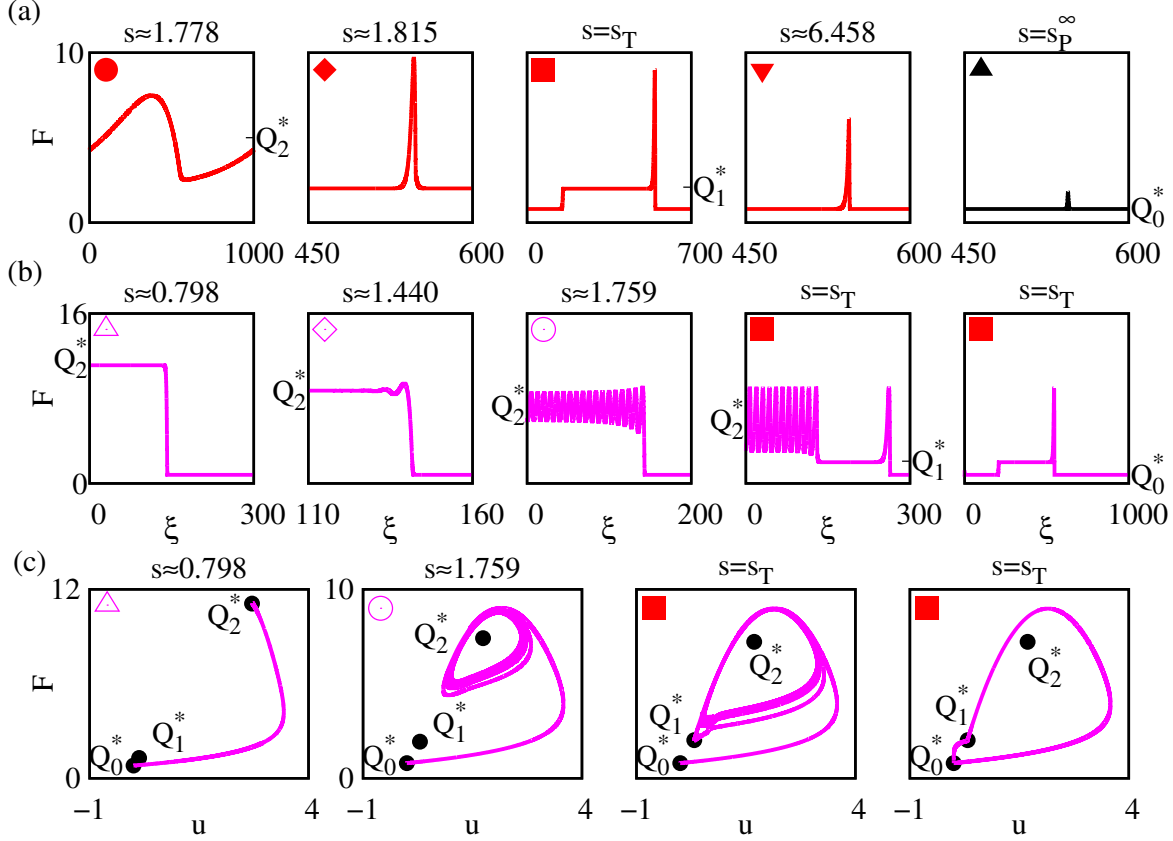
Figure 7: Solution profiles at selected locations in Figure 6 along the (a) EP and (b) TF branches, where for visibility, we do not always show the whole domain length of $L = 1000$. Here $(s_T, s_P^\infty) \approx (1.804, 1.167)$ are defined as in Figure 6. (c) Selected phase space projections of the TFs (heteroclinic orbits) showing the transition to EPs (homoclinic orbits). Note that the EPs and TFs are all non-negative for each solution component.

order of bifurcations differs from the one discussed in [66], where excitable pulses were found to emerge from a global T-point bifurcation and connect to the HB of homogeneous steady states (HSSs). The latter resembles the case with $M = 4.5$ (see Figure 3b). Therefore, we focus first on coherent solutions for $M = 4.5$ using a domain length of $L = 1000 \gg \lambda \approx 3.09$ to approximate an infinite domain. The coherent solutions include excitable pulses (EPs) and travelling fronts (TFs), both propagating as spatially localized states corresponding to homoclinic and heteroclinic connections in phase space, respectively, and stationary wave-pinning (WP) solutions. Then, we show the fundamental difference between the $M = 4.5$ and $M = 2$ cases, concerning the instability and stability of WPs, respectively.

We demonstrate first the results for $M = 4.5$, $L = 1000$, and $b = 0.00067$, in Figure 6, noting that we confirmed persistence at other values of b. The instability of the HSS Q_2^* is a finite wavenumber Hopf bifurcation (WB at $s = s_c^t$). As s increases, subsequent bifurcations
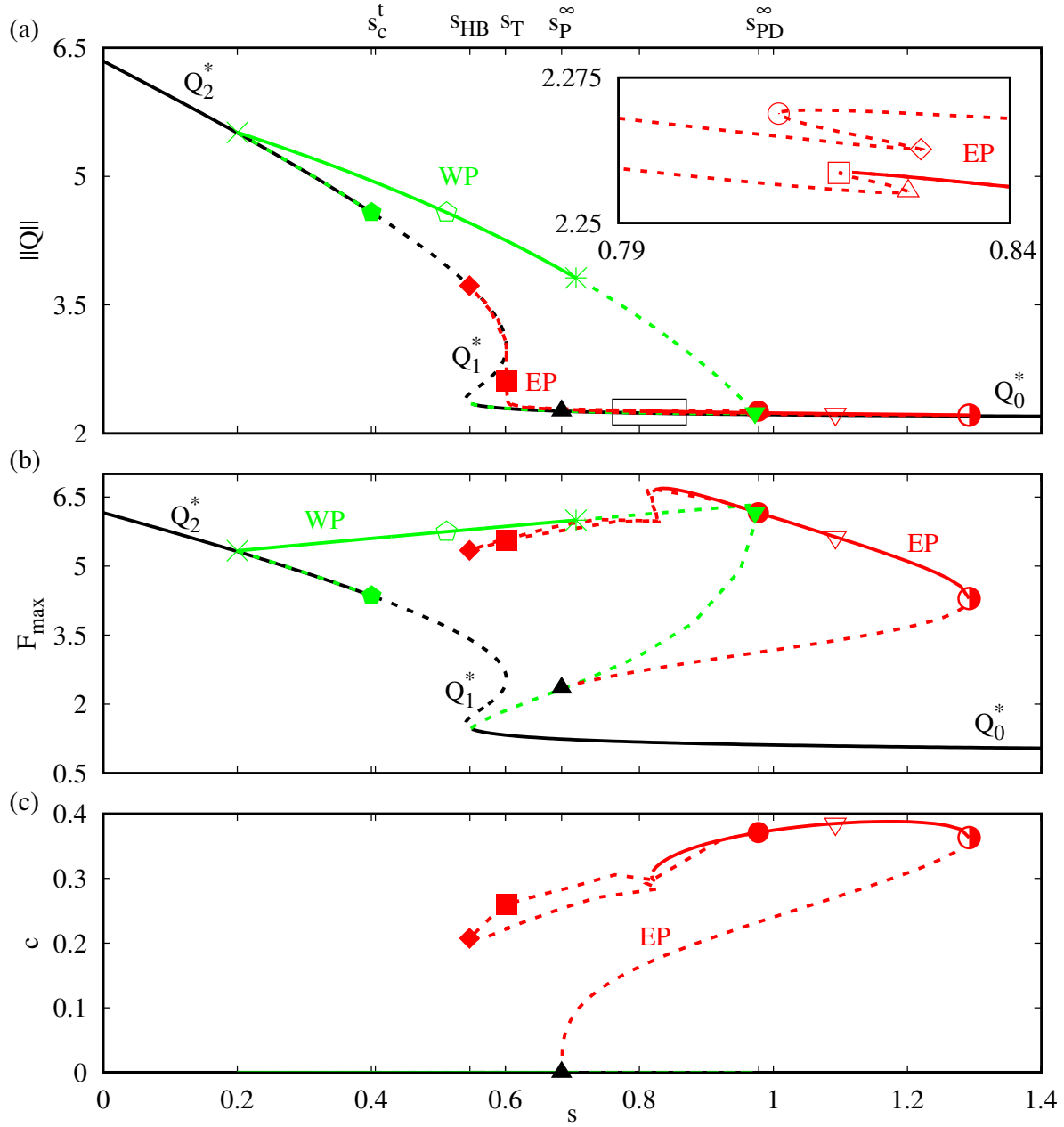
Figure 8: Bifurcation diagrams computed via numerical continuation as a function of s, showing excitable pulses (EPs), wave-pinning (WP) solutions, and the homogeneous steady states $Q^*_{0,1,2}$ for $M = 2$ and $L = 1000 \gg \lambda \approx 3.09$ (where λ is the wavelength leading to instability of Q^*_2). The solution branches are projected with the Sobolev norm (5.1) in (a), the maximum value of F in (b), and the propagation speed in (c); solid (dashed) lines denote linearly stable (unstable) solutions. In contrast to the $M = 4.5$ case (cf. Figure 6), WP solutions stabilize over a finite region and excitable pulses emerge only from a parity-breaking bifurcation (black triangle) of WP solutions at $s = s^\infty_P$. The inset in (a) shows the locations of several folds along the EP branch that are invisible, otherwise. The critical values $(s^t_c, s_{HB}, s_T, s^\infty_P, s^\infty_{PD}) = (0.406, 0.565, 0.602, 0.684, 0.978)$ denote the codimension-2 long wavelength (LW)/finite wavenumber Hopf bifurcation (WB), the homogeneous Hopf (HB), the T-point bifurcation (red square), and the parity-breaking (black triangle) and period-doubling (red circle) bifurcations of EPs, respectively. The symbols (circle, diamond, etc.) represent selected locations of solution profiles given in Figure 9. Other parameter values as in Table 1 with $b = b_c \approx 0.067$.
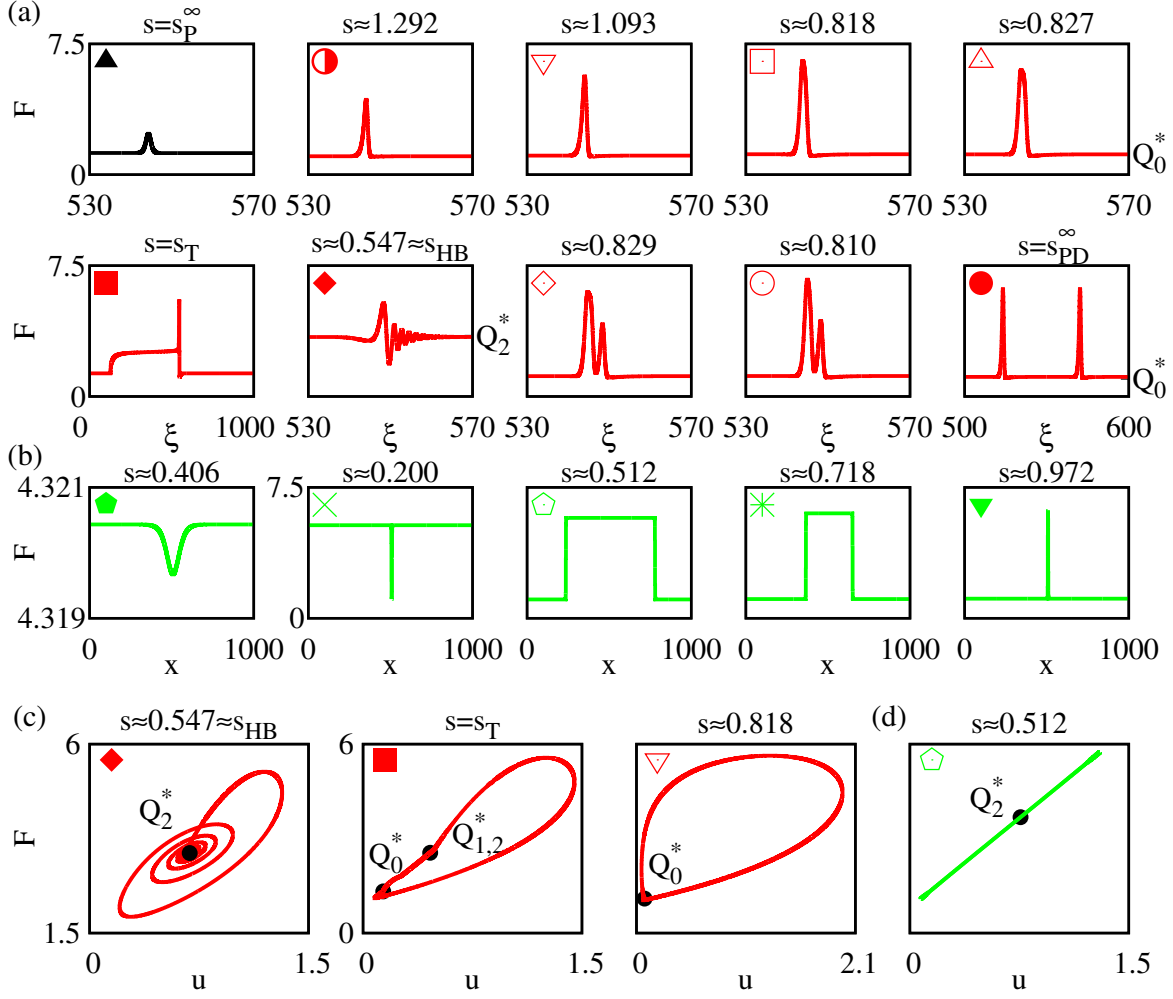
Figure 9: Solution profiles at selected locations in Figure 8 along the (a) EP and (b) WP branches, where for visibility, we do not always show the whole domain length of $L = 1000$. Here $(s_{HB}, s_P^\infty, s_T) \approx (0.565, 0.684, 0.602)$ are defined as in Figure 8. Selected phase space projections are shown for EPs in (c) and WP solutions in (d), where in (d) only the homogeneous steady state Q_2^* exists.

are observed: uniform Hopf (HB at $s = s_{HB}$), followed by a long wavelength (LW at $s = s_{LW}^t$). As in [66] and in Appendix B, near the HB, these are broad periodic solutions with a wavelength matching the domain size (circle). They become unstable EPs bi-asymptotic in space to Q_1^* (i.e., as $\xi \to \pm\infty$) through a homoclinic bifurcation (diamond), then become stable EPs to Q_0^* after the global T-point bifurcation (at $s = s_T$, square), and finally, after an additional fold, terminate as unstable EPs at the parity-breaking bifurcation of WP states ($s = s_P^\infty$, triangle). The solution profiles are shown in Figure 7a. The WP solutions bifurcate
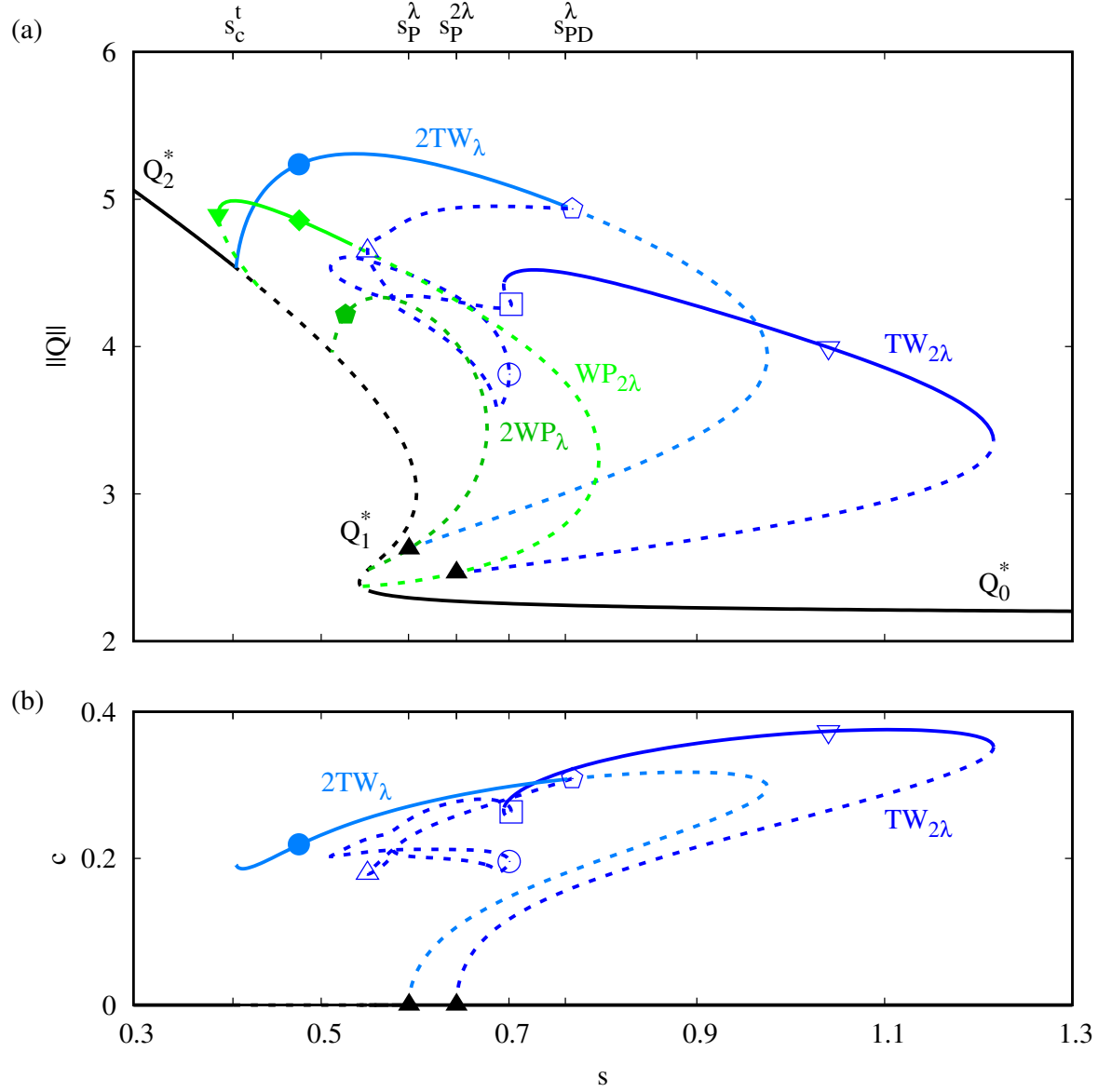
Figure 10: Bifurcation diagrams computed via numerical continuation as a function of s, showing the homogeneous steady states $Q_{0,1,2}^*$, and travelling waves (TWs) and wave-pinning (WP) solutions with wavelengths λ and 2λ for $M = 2$ and $L = 2\lambda \approx 2 \cdot 3.09$ (where λ is the critical wavelength at the instability onset of Q_2^*). The solution branches are projected with the Sobolev norm (5.1) in (a) and the propagation speed in (b); solid (dashed) lines denote linearly stable (unstable) solutions. The notation $2TW_\lambda$ denotes two spatial copies of travelling waves with wavelength λ. Here, TWs and WP solutions form a bistable region with wavelengths λ and 2λ, respectively. The critical values $(s_c^t, s_P^\lambda, s_P^{2\lambda}, s_{PD}^\lambda) = (0.406, 0.593, 0.664, 0.760)$ denote the codimension-2 long wavelength (LW)/finite wavenumber Hopf (WB) onset, the parity-breaking bifurcations (black triangles) at wavelengths λ and 2λ, respectively, and the period-doubling (hollow pentagon) bifurcation of λ. The symbols (circle, diamond, etc.) represent selected locations of solution profiles given in Figure 11. Other parameter values as in Table 1 with $b = b_c \approx 0.067$.
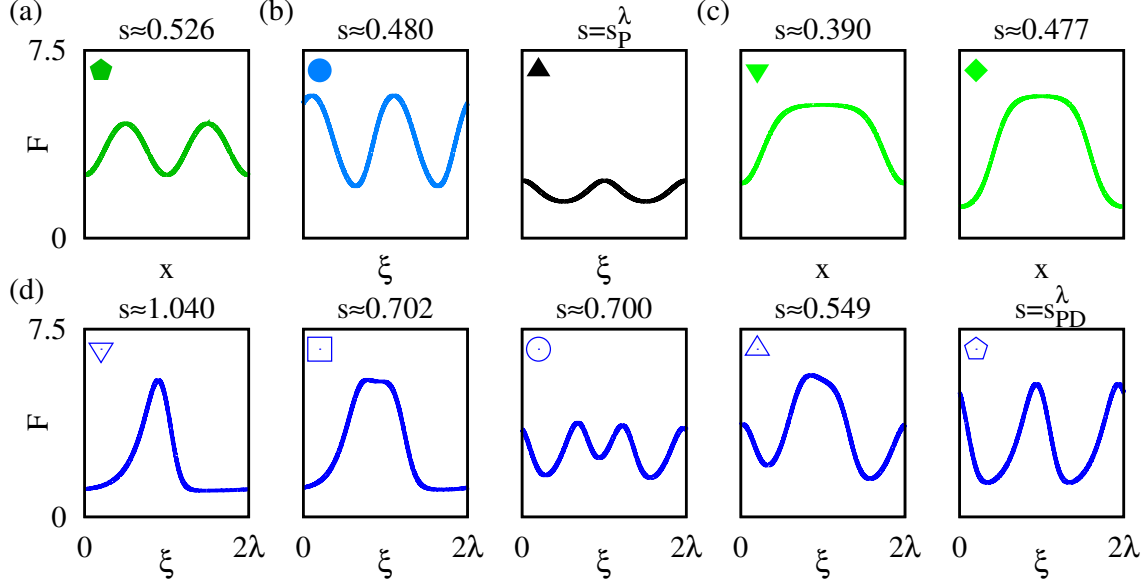
Figure 11: Solution profiles at selected locations in Figure 10 along the branches (a) $2WP_\lambda$ (b) $2TW_\lambda$ (c) $WP_{2\lambda}$, and (d) $TW_{2\lambda}$. Here $(s_P^\lambda, s_{PD}^\lambda) \approx (0.593, 0.760)$ are defined as in Figure 10.

subcritically about Q_2^* and Q_0^* (at $s = s_{LW}^t \approx 2.044$ and $s = s_{LW}^b \approx -0.661$, respectively). The bifurcating solutions are of a single wavelength, becoming spatially localized as we move along the branch away from their onset. These solutions always remain unstable. Further details about WP solutions will be given later in the discussion of the $M = 2$ case.

For completeness, we also indicate that in the regime $s_c^b < s < s_c^t$, there is bistability between the HSSs Q_0^* and Q_2^* (see Figure 6), which gives rise to TFs. Below the WB instability, s_c^t, fronts connecting Q_0^* and Q_2^* exhibit monotonic bi-asymptotic spatial decay and are linearly stable, whereas for $s > s_c^t$, the fronts are unstable while exhibiting spatially decaying oscillations about Q_2^*. Above s_c^t, these oscillations extend, forming a heteroclinic connection between a spatially periodic orbit and Q_0^*. Additional increase in s leads to a connection between two double-heteroclinic solutions collapsing at a T-point, s_T: (i) periodic-Q_1^*-Q_0^* and (ii) Q_0^*-Q_1^*-Q_0^*. We demonstrate the two double heteroclinic profiles in Figure 7b (see square), and in Figure 7c, we show the respective phase portrait projections.

Next, in Figures 8 and 9, we show that the bifurcation structure of coherent solutions for $M = 2$ is qualitatively different from that of $M = 4.5$. When $M = 2$, EPs bifurcate from WP solutions in a parity-breaking bifurcation at $s = s_P^\infty$ (triangle), stabilize after the first fold (homoclinic connections of Q_0^*, right semicircle) and destabilize at the subsequent left fold (hollow square). Then, the branch folds again before reaching a T-point bifurcation (square) at $s = s_T$ (see Figure 9a). Here, the solutions form a homoclinic cycle with Q_0^* at the saddle-node, i.e., the solutions briefly plateau at $Q_2^* = Q_1^*$ (see square in Figure 9c). Afterwards, the branch proceeds to the left and folds as a Shil'nikov homoclinic connection to Q_2^* (diamond), see also the phase portrait projection in Figure 9c. Then, the branch passes the T-point again,

where an additional peak appears. The branch associated with a bounded two-peak state goes through two more folds (hollow diamond and circle), after which the peaks start to separate until reaching equidistance, and thus, the branch terminates in a period-doubling bifurcation at $s = s_{PD}^\infty$; we omit the EP branch with wavelength $L = 500$ as the branch is effectively the same as with wavelength $L = 1000$. Note that similar bifurcation structures related to peak doubling near T-point bifurcations have also been observed in an RD model but in the absence of mass conservation [35].

Finally, we address the WP branch that bifurcates from $s = s_c^t$. As with high mass ($M = 4.5$), the solutions emerge subcritically from Q_2^* and Q_0^* but these onsets are instabilities when $M = 2$. For both masses, the solutions bifurcate as single wavelength states and become localized as s changes from the onsets up to the folds. From Q_2^* these resemble holes and from Q_0^* peaks, see Figure 9b. After the folds, the hole and the peak widen, where s controls the width of the WP solutions. Hence, in between the two folds, the solutions form a homoclinic-like cycle, resembling two locked fronts. However, both plateaus are not HSS of the system, as shown for mass-conserved systems in [57] and seen by the profile and phase-portrait projection marked by the hollow pentagon in Figure 9b,d. Stability computations show that the WP solutions are linearly stable from the left fold and up to $s \approx 0.718$, see Figure 8.

In summary, the analysis for large domains in this section reveals a nontrivial organization of coherent solutions depending on the mass M of the (u, v)-subsystem. Our key result for large domains is that WP solutions are linearly stable for low mass ($M = 2$). This result enables our investigation into the stable coexistence of WP with travelling waves. We next consider domains of moderate size.

5.2. Coexistence and bistability for moderate domain size, $L \sim \mathcal{O}(m\lambda)$. We now analyze a domain whose size is consistent with biological cells, namely much smaller domains than the large domain size in Subsection 5.1. We keep the same parameter values as in Figure 8. Since the primary bifurcation is the codimension-2 long wavelength/finite wavenumber Hopf instabilities (LW/WB), we choose the critical wavelength $\lambda \approx 3.09$ as a characteristic scale and the minimal wavelength of interest. We consider two cases, with domain lengths $L = 2\lambda$ (Figure 10) and $L = 3\lambda$ (Figure 12). In each case, we show WP and TW solutions with wavelength L and $L/2$. Thus, the critical TW branch (TW_λ) is shown with domain length $L = 2\lambda$. For all bifurcation diagrams on finite domains, we compute the stability of solutions for the largest domain length, unless otherwise stated. Therefore, solutions with smaller wavelengths are periodically extended to fit into the domain. This does not affect the curve of solutions but does change the linear stability onset along the branch. A notation of the form $2TW_\lambda$ is used to indicate the travelling wave branch with wavelength λ and 2 spatial copies.

Results for domain length $L = 2\lambda$ are summarized in Figures 10 and 11. The $2WP_\lambda$ solutions emerge for $s > s_c^t$ supercritically, due to finite size effects, and remain unstable until the branch terminates about Q_1^*, i.e., these solutions do not terminate at Q_0^* like the WP solutions in large domains. The instability of WP solutions on small domains is unsurprising, cf. [46]. The $2TW_\lambda$ branch is supercritical (as shown in Section 4), initially linearly stable, loses stability at $s = s_{PD}^\lambda$, and after a subsequent fold terminates at a parity-breaking bifurcation at $s = s_P^\lambda$. The TWs with wavelength 2λ, however, are much different and resemble the structure of the EP branch. The solutions emerge from a parity-breaking bifurcation at $s = s_P^{2\lambda}$ of
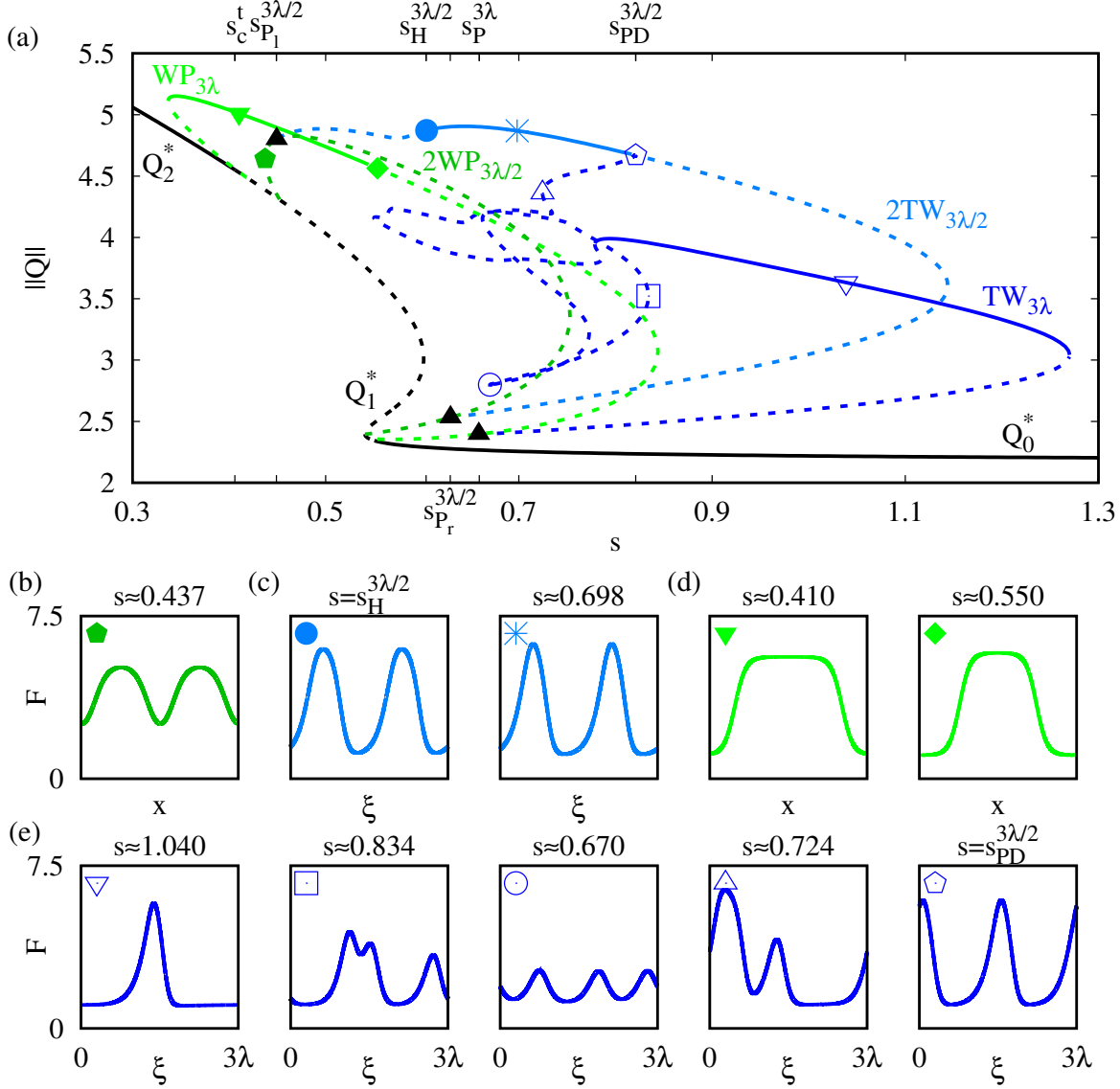
Figure 12: (a) Bifurcation diagram computed via numerical continuation as a function of s, showing the homogeneous steady states $Q_{0,1,2}^*$, and travelling waves (TWs) and wave-pinning (WP) solution branches with wavelengths $3\lambda/2$ and 3λ for $M = 2$ and $L = 3\lambda \approx 3 \cdot 3.09$ (where λ is the critical wavelength at the instability onset of Q_2^*). Here we only show projections with the Sobolev norm (5.1); solid (dashed) lines denote linearly stable (unstable) solutions. The notation $2TW_{3\lambda/2}$ denotes two spatial copies of TWs with wavelength $3\lambda/2$, where the onsets of each one of the solution branches are at the respective parity-breaking bifurcations. The critical values are $(s_c^t, s_{P_l}^{3\lambda/2}, s_{P_r}^{3\lambda/2}, s_P^{3\lambda}, s_H^{3\lambda/2}, s_{PD}^{3\lambda/2}) = (0.406, 0.449, 0.629, 0.659, 0.604, 0.821)$, for the codimension-2 long wavelength (LW)/finite wavenumber Hopf (WB) bifurcation, the parity-breaking bifurcation at wavelengths $3\lambda/2$ on the left and right, and 3λ, respectively, and the Hopf (H) and period-doubling bifurcations of $TW_{3\lambda/2}$. (b-e) Selected solution profiles for (b) $2WP_{3\lambda/2}$ (c) $2TW_{3\lambda/2}$ (d) $WP_{3\lambda}$ and (e) $TW_{3\lambda}$ at corresponding points marked in (a). Other parameter values as in Table 1 with $b = b_c \approx 0.067$.

respective WP solutions, gain stability at the subsequent fold, and then lose stability at the next. Afterwards, the solutions transition to multiple peak solutions at the subsequent folds. In particular, we see that initially, the plateau of the peak expands (hollow square), then transitions into three-peak (hollow circle), and then into two-peak (hollow triangle) solutions but with different amplitudes and spacings. Finally, the branch reaches a period-doubling bifurcation (as seen with EPs) at $s = s_{PD}^{\lambda}$, where the $2TW_\lambda$ branch loses stability. The $WP_{2\lambda}$ branch resembles the bifurcation structure obtained for WP solutions in large domains: WP solutions emerge from Q_2^* towards decreased s values, and after the left fold, they gain stability, before reaching a subsequent fold and terminating at Q_0^*. Consequently, on domain size $L = 2\lambda$, WP solutions stably coexist with TWs of two copies.

Increasing the domain length to $L = 3\lambda$ introduces distinct bifurcation structures for TWs and WP solutions as shown in Figure 12, but also has many similarities. First, the $WP_{3\lambda}$ branch has a similar structure to the $WP_{2\lambda}$ branch. However, the $TW_{3\lambda}$ branch, which also emerges from a parity-breaking bifurcation of the $WP_{3\lambda}$ branch, goes through slightly different transitions from stable $TW_{3\lambda}$ to the period-doubling bifurcation of $TW_{3\lambda/2}$ at $s = s_{PD}^{3\lambda/2}$. In particular, the transition to a three-peak solution (hollow circle) requires an additional fold (hollow square) and the solution at the final fold before the period-doubling bifurcation is more localized with a broad trough (hollow triangle), as seen with the EPs. The $2TW_{3\lambda/2}$ branch does not emerge from Q_2^*. Instead, these TWs emerge from two parity-breaking bifurcations, both from the $2WP_{3\lambda/2}$ branch (which is everywhere unstable). On the right, at $s = s_{P_r}^{3\lambda/2}$ the parity-breaking bifurcation is similar to the previous TW branches, including the stability change at $s = s_{PD}^{3\lambda/2}$. However, these TWs lose stability in a Hopf bifurcation and terminate on the left, at an additional parity-breaking bifurcation, $s = s_{P_l}^{3\lambda/2}$. When $L = 3\lambda/2$, $TW_{3\lambda/2}$ remains stable until the parity-breaking bifurcation at $s = s_{P_l}^{3\lambda/2}$ and $WP_{3\lambda/2}$ is stable between the initial fold (as with other WP branches) and the parity-breaking bifurcation. Therefore, a smooth transition from stable WP to TW solutions is observed when $L = 3\lambda/2$.

Consequently, the most important outcome here is that multiple copies of TWs form a bistable region with WP solutions for a broad range of parameters and domain lengths, even though the bifurcation structure may differ in each case.

6. Pattern selection using time-dependent simulations. The bifurcation structures explored in Section 5 provide information on the types of solutions and their linear stability for various domain sizes L and masses M of the (u, v)-subsystem. These results do not yet inform us on the relative basins of attraction of the stable solutions, nor how they interact and compete. To explore these questions, we numerically integrate (2.3) (for details see Appendix A.3). We select initial conditions (ICs) that represent combinations of solution types and/or large amplitude perturbations: that is, we take combinations of stable WP and TW solutions with domain lengths 3λ, i.e., picking each from the $WP_{3\lambda}$ and $3TW_\lambda$ stable regime (see Figure 13). For each simulation, we only show the F-actin concentration, F; however, the active GTPase u is also important in these perturbations as $u = 0$ means there is locally no F-actin feedback to the GTPase. In Appendix A.3, we show that the profiles of the other solution components are qualitatively similar and all non-negative.
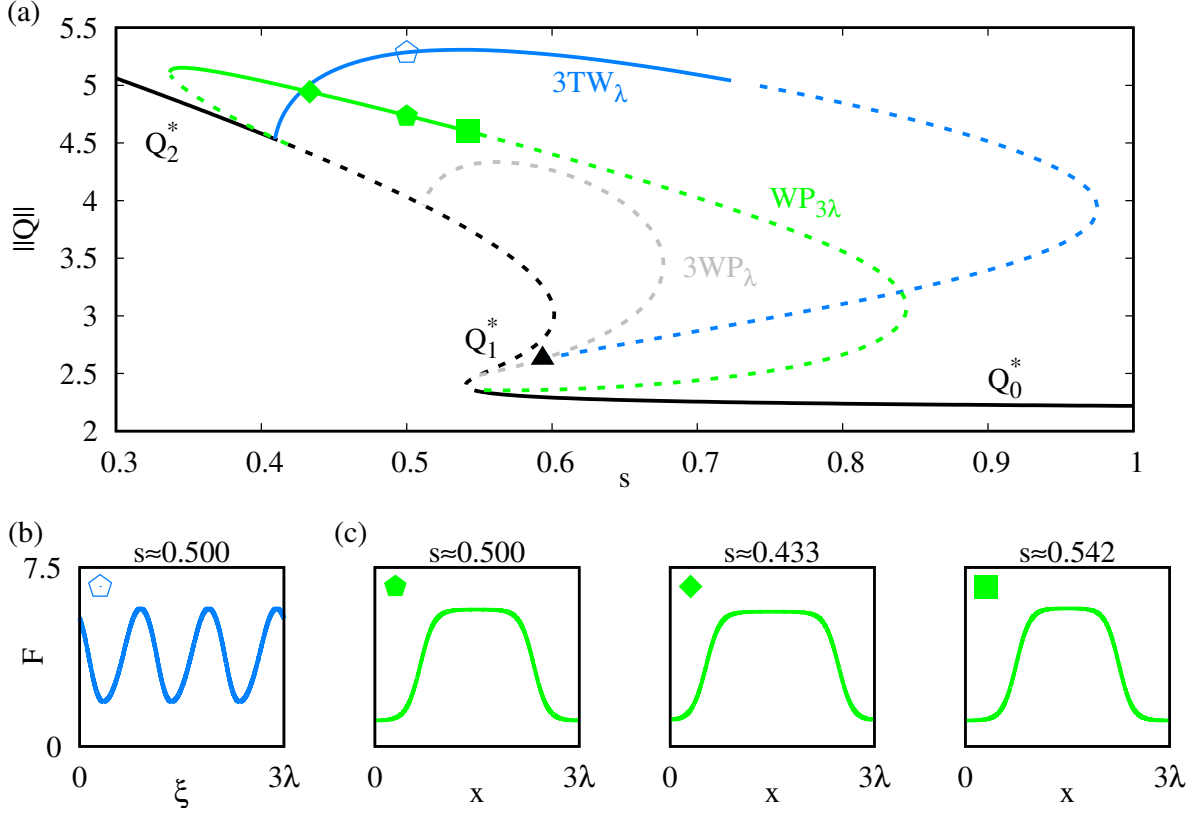
Figure 13: (a) Bifurcation diagrams computed via numerical continuation as a function of s, showing the homogeneous steady states $Q^*_{0,1,2}$, travelling waves (TWs) with wavelength λ, and wave-pinning (WP) solutions with wavelengths λ and 3λ for $M = 2$ and $L = 3\lambda \approx 3 \cdot 3.09$, where λ is the wavelength at the instability onset of Q^*_2. The solution branches are projected with the Sobolev norm (5.1); solid (dashed) lines denote linearly stable (unstable) solutions. The notation $3TW_\lambda$ denotes three spatial copies of TWs with wavelength λ. Note that the loss of stability for both $WP_{3\lambda}$ and TW_λ is via Hopf bifurcations. The symbols (diamond, pentagon, square) denote locations of solutions used as components of initial conditions (ICs) in direct time-dependent simulations of (2.3). (b,c) Solution profiles in F at locations indicated in (a), see also Figure 18a-d for all solution components. Pentagons indicate ICs for Figure 14 while other symbols are used as ICs in Figure 17. Parameter values as in Table 1 with $M = 2$ and $b = b_c \approx 0.067$.

6.1. Initial superposition of wave-pinning and travelling wave states, $L = 3\lambda$. Setting $s = 0.5$ (pentagons in Figure 13), we use ICs that superimpose the WP and TW solutions in the convex combination,

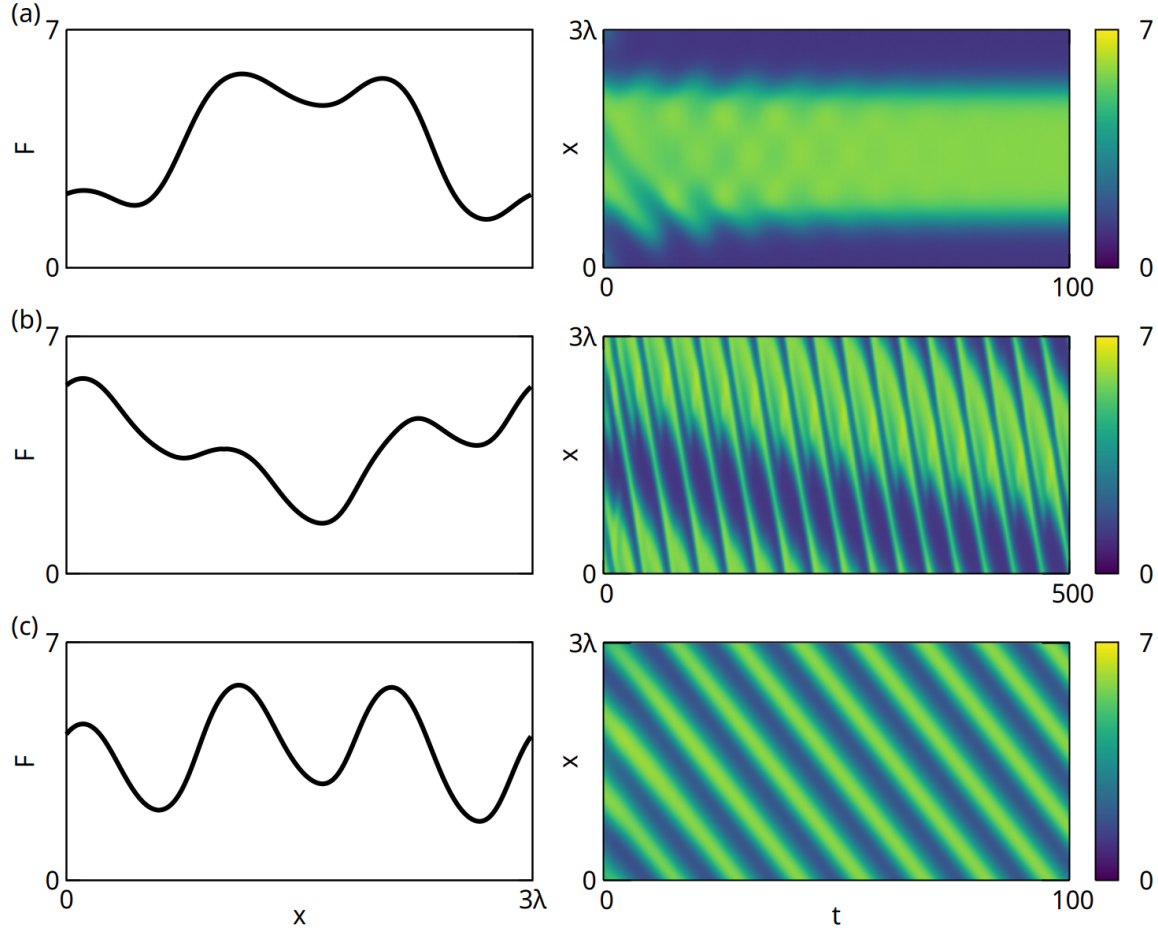$$(6.1) \qquad\qquad Q_{IC}(x) = \delta Q_{TW}(x) + (1 - \delta)Q_{WP}(x),$$

Figure 14: Direct numerical integration of (2.3) with periodic boundary conditions, initialized with a convex combination (6.1) of wave-pinning and travelling waves (left panels). Spacetime plots ("kymographs", right panels) showing F as a heat map for (a) $\delta = 0.25$, (b) $\delta = 0.5$, and (c) $\delta = 0.75$. In (b), we demonstrate a distinct kind of modulated solution that persists also at a much longer simulation time, $t = 50000$; see also a supplementary movie_Fig14b. Parameter values as in Table 1 with $M = 2, b = b_c \approx 0.067$, $s \approx 0.50$, and $L = 3\lambda \approx 3 \cdot 3.09$.

with $0 \leq \delta \leq 1$ as a weighting parameter. Figure 14 shows ICs with $\delta = 0.25, 0.5, 0.75$ (left) and space-time plots (a.k.a. kymographs, right) of the ensuing dynamics of F. As expected, the time-dependent simulation converges to the solution that is weighted more heavily in the IC. When the WP solution dominates ($\delta < 0.5$, Figure 14a), oscillations induced by the TW linger for a while, but are eventually damped out. For $\delta > 0.5$ (Figure 14c), where TWs initially dominate, convergence to the pure TW solution is almost immediate. The weighting $\delta = 0.5$ (Figure 14b) leads to an exotic solution resembling a modulated travelling wave. However, one of the two peaks widens and splits, emanating an additional wave that dampens along the
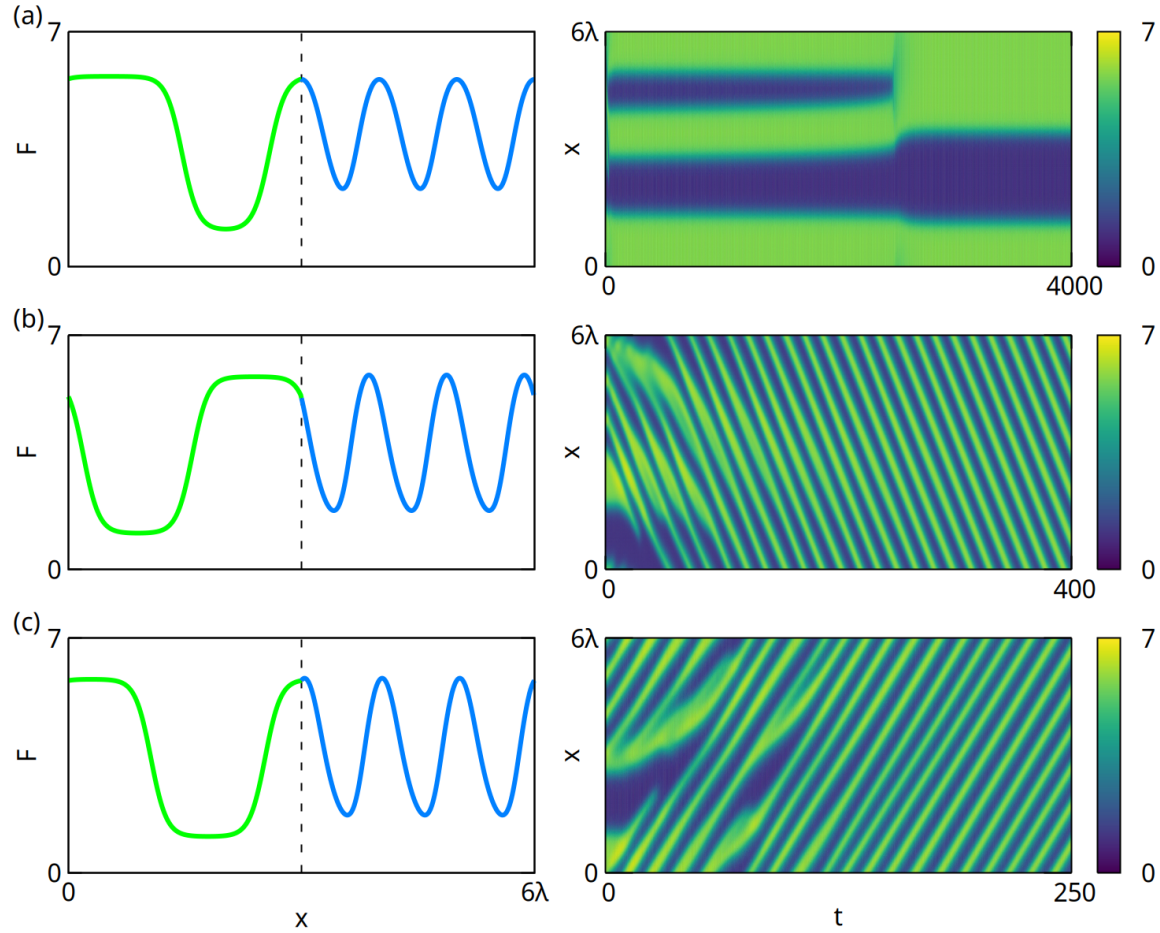
Figure 15: Direct numerical integration of (2.3) with periodic boundary conditions, initialized with wave pinning (WP) solutions and 3-period travelling waves (TWs) of wavelength λ, on adjoining parts of the same domain (left panels). Spacetime plots (right panels) showing F as a heat map for (a) $s \approx 0.45$, (b) $s \approx 0.52$, and (c) $s \approx 0.53$. In (b) the asymptotic TWs are with a wavelength of $6\lambda/5$. Parameter values as in Table 1 with $M = 2, b = b_c \approx 0.067$, and $L = 6\lambda \approx 6 \cdot 3.09$.

leading edge of the original peak (see supplementary movie_Fig14b). This behaviour persists for a long time ($t \approx 50000$), but we cannot assure it is an asymptotic solution. Therefore, complex time-dependent solutions and/or long transients are also possible.

6.2. Initial fronts of wave-pinning and travelling wave states, $L = 2 \cdot 3\lambda$. Next, we consider interactions of TWs with WP solutions when they are initially in adjoining parts of the domain. We considered the effect of the parameter s (which, recall, controls the width of the WP plateau) on the ability of TWs to invade and dominate. As shown in Figure 15, initial conditions (Q_{IC}) combine a WP solution (on $0 < x < 3\lambda$) glued continuously to a TW
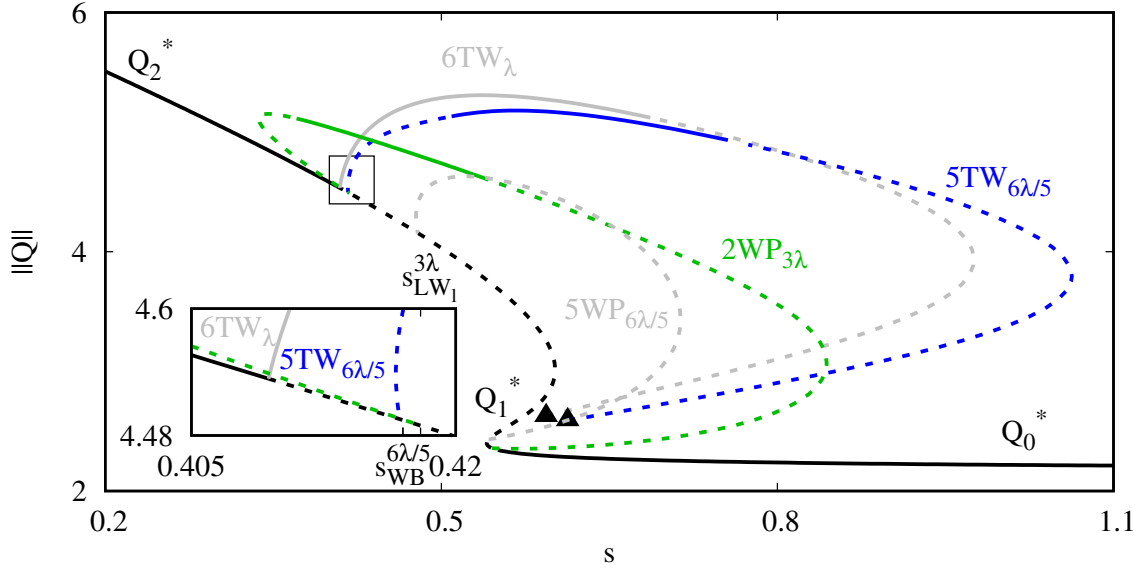
Figure 16: Bifurcation diagram computed via numerical continuation as a function of s, showing the homogeneous steady states $Q_{0,1,2}^*$ and the secondary solutions found in Figure 15a,b, with $L = 6\lambda \approx 6 \cdot 3.09$, where λ is the wavelength at the instability onset of Q_2^*; solid (dashed) lines denote linearly stable (unstable) solutions. We showcase two-copies of $WP_{3\lambda}$ ($2WP_{3\lambda}$, green) and five-copies of $TW_{6\lambda/5}$ ($5TW_{6\lambda/5}$, blue). The inset shows a zoom into the bifurcation onsets, where both $2WP_{3\lambda}$ and $5TW_{6\lambda/5}$ are subcritical. The labels $(s_{WB}^{6\lambda/5}, s_{LW_l}^{3\lambda}) \approx (0.417, 0.418)$ denote the s-values of the onset from Q_2^* of the $TW_{6\lambda/5}$ and $WP_{3\lambda}$ branches, respectively. For comparison, we also plot the typical TW_λ branch and the reference $WP_{6\lambda/5}$ (both in gray). Parameter values as in Table 1 with $M = 2$ and $b = b_c \approx 0.067$.

(on $3\lambda < x < 6\lambda$). We picked values of $s \approx 0.45, 0.52, 0.53$ (above s_c^t), according to:

(6.2)
$$Q_{IC}(x) = \begin{cases} Q_{WP}(x) & x \leq 3\lambda \\ \begin{pmatrix} u_{TW}(x - \rho_1) \\ v_{TW}(x - \rho_2) \\ F_{TW}(x - \rho_3) \end{pmatrix} & x > 3\lambda \end{cases}$$

where Q_{WP} and Q_{TW} are pure WP and 3-period TWs with wavelength λ. The values of spatial shifts, $\rho_{1,2,3}$, are chosen so that Q_{IC} are continuous.

For $s = 0.45$, TWs are rapidly damped, and a transient coarsening (of about 2500 time units) [36] takes place before a single-plateau WP solution emerges (Figure 15a). For $s = 0.52$, we find that TWs rapidly take over (see Figure 15b), however, the asymptotic wavelength is $6\lambda/5$. For $s \approx 0.53$, TWs also persist and the wavelength λ is retrieved. We note that the choice of wavelengths depends on the initial condition (i.e. the shifting parameters $\rho_{1,2,3}$).
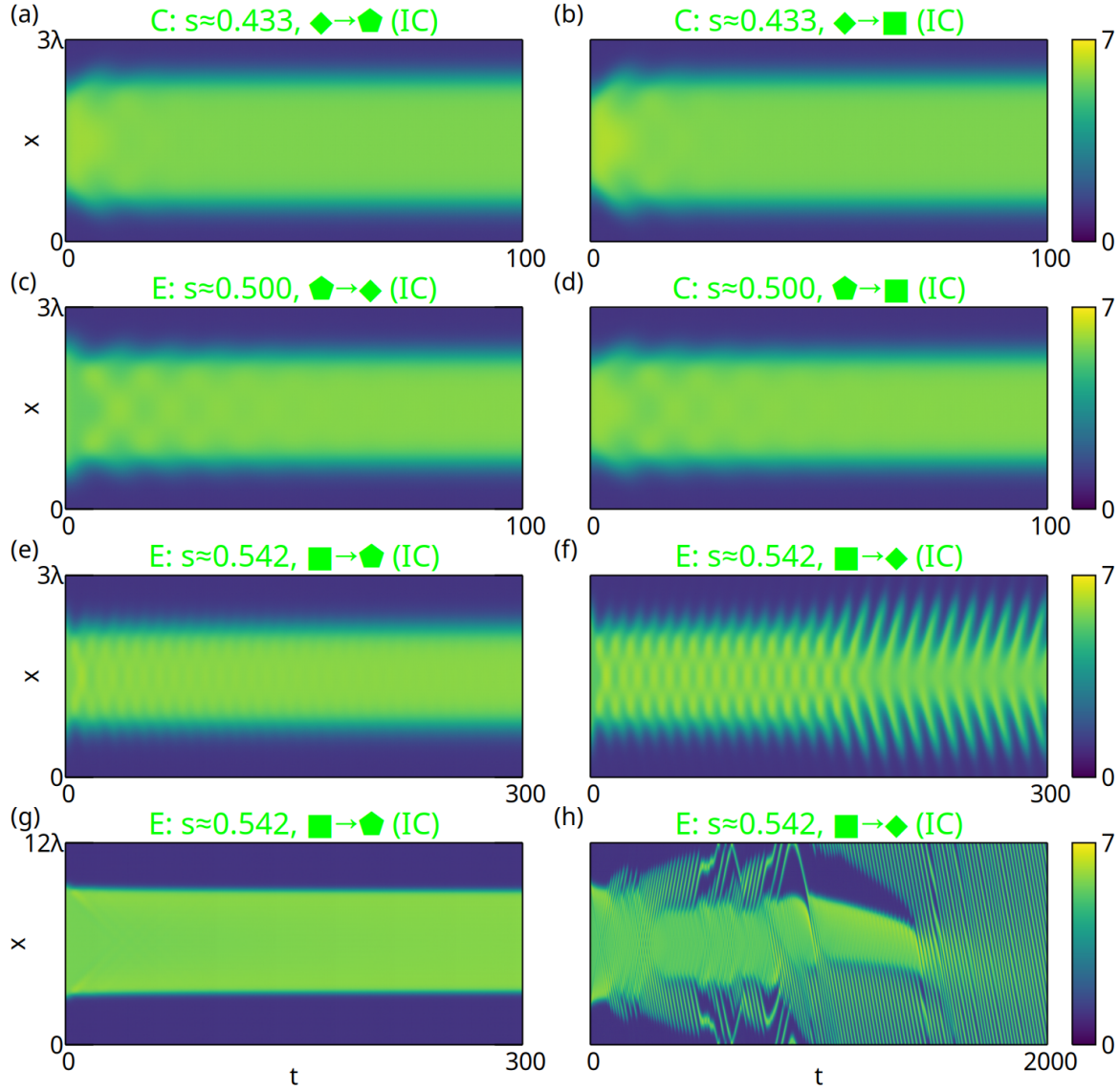
Figure 17: (a-h) Spacetime plots showing F as a heat map obtained via direct numerical integration of (2.3) with periodic boundary conditions, initialized with wave pinning (WP) solutions obtained from selected locations given by symbols in Figure 13. The first letter in the titles denotes the type of numerical experiment: compression (C) and expansion (E) with respect to the steady-state WP solution at the given s value. The symbols ◆ → ■ in the titles correspond to selected locations in Figure 13, where the parameter values are given by ◆ and the initial condition is ■. The profiles of each component of the initial conditions are given in Figure 18a-d of Appendix A.3. Parameter values as in Table 1 with $M = 2$, $b = b_c \approx 0.067$, and (a-f) $L = 3\lambda \approx 3 \cdot 3.09$ and (g,h) $L = 12\lambda \approx 12 \cdot 3.09$, see also the supplementary movie_Fig17f for (f).

Motivated by numerical simulations in Figure 15a,b, we plot a bifurcation diagram (Figure 16) showcasing the two-copies of $WP_{3\lambda}$ (green) and five-copies of secondary travelling waves of $TW_{6\lambda/5}$ (blue), respectively. As can be seen from Figure 16, $2WP_{3\lambda}$ is stable at $s = 0.45$ but the intermediate solution in Figure 15a is a bimodal WP solution with differing wavelengths and is thus not two copies of a $WP_{3\lambda}$ solution. The TW solution with wavelength $6\lambda/5$ is one of the secondary TWs bifurcating for $s > s_c^t$ (Figure 16). For completeness, we also plot the $WP_{6\lambda/5}$ branch, noting that it emerges from Q_1^* (as does the WP_λ branch). The branch $TW_{6\lambda/5}$, however, has notable differences from the critical branch (TW_λ): it is subcritical rather than supercritical and does not gain stability at the initial fold (inset, Figure 16). This implies that the stability region is entirely contained on the upper branch, bounded away from the folds. This follows the expected behaviour of TWs that emerge from secondary bifurcations (see supplementary materials of [66]). We also see that TWs with wavelength $6\lambda/5$ follow the primary branch of bifurcating TWs (TW_λ), meaning the branch connects the secondary finite wavenumber Hopf and the parity-breaking bifurcations (see Figure 16).

6.3. Robustness of wave-pinning states. A key characteristic of a WP solution is the plateau width, corresponding to F-actin. From Section 5, we know that the plateau width of the WP solutions is controlled by s. So here, we address the role of large (nonlinear) perturbations of WP solutions following changes in the width of the plateau by employing ICs representing compression or expansion of the WP plateau. For ICs, we use the parameter values and corresponding WP solutions at the diamond, pentagon, and square on the stable portion of the $WP_{3\lambda}$ branch in Figure 13 and simulate all possible permutations of distinct parameter sets. This construction preserves the value of M (and all other parameters).

Figure 17a-f showcases the six simulations generated from all possible permutations of initial conditions and parameter sets with $L = 3\lambda$. Note that the square represents a solution close to the onset of the $WP_{3\lambda}$ Hopf instability. Figure 17a-d show that WPs persist for s values away from the instability (diamond and pentagon). Note that this behaviour persists for initial conditions along the entire stable portion of the WP branch (i.e., to the left fold of the $WP_{3\lambda}$ branch in Figure 13). However, Figure 17f shows that near the instability (square) the WP solution is lost with a large enough perturbation. The emergent behaviour is initially of small amplitude standing waves (SWs), which at later times ($t \gtrsim 150$) destabilize and become modulated TWs. This behaviour was verified but not shown with slightly smaller s values and ICs to the right of the square in Figure 13. We repeated the experiments (e,f) but with a domain length of $L = 12\lambda$, as shown in (g,h); note that for $L = 12\lambda$ the instability of WPs is at $s \approx 0.574$. Integration shows a similarity between (e,f) and (g,h), although in (h) we observe richer dynamics than in (f), which is expected in increased domain sizes. Since the Hopf instability onset of WP solutions in $L = 12\lambda$ is at higher s values, we attribute the instability to the nature of the perturbations (possibly due to subcriticality of the Hopf bifurcation) resulting from the dynamics of leading eigenfunctions near the Hopf onset rather than from the proximity to the onset location. The complex conjugated eigenfunctions (see Appendices A.1 and A.3) indeed show pronounced contributions at the WP top plateau region, where SW-like dynamics are observed. Hence, these numerical results suggest that WP solutions increase their robustness if they are closer to the left fold, i.e., wider top plateaus.

7. Conclusions. We analyzed a mass-conserving reaction-diffusion (RD) model (2.3) on a 1D domain with (mostly) periodic boundary conditions mimicking a ring of the actin cortex at the edge of a cell. Bifurcation analyses (see Sections 3 to 5) reveal a rich structure of possible solutions depending not only on control parameters but also on the total mass M of the (u, v)-subsystem. We prescribe the conditions in which steady wave-pinning (WP) solutions (a.k.a. cell polarization) can stabilize and coexist with stable travelling waves (TWs). Specifically, we unfold the bifurcations about a codimension-2 long wavelength (LW) and finite wavenumber Hopf (WB) instability and show how these depend on the domain length. We note, however, that the main results qualitatively persist and are not subject only to the codimension-2 LW/WB instability.

By studying solutions with distinct spatial scales, we showcase the important role of domain size in selecting the kinds of patterns that can emerge. In large domains (see Figures 6 and 8), we showed that the stability regions of WP solutions and excitable pulses (EPs) are well separated in parameter space (see Figure 8), regardless of M values. This separation is generic, since WP solutions with stable regions primarily bifurcate subcritically in a decreasing s direction, whereas EPs bifurcate in a parity-breaking bifurcation towards increasing s. (This was confirmed, but not shown in other parameter regimes.) The fact that both EPs and WP solutions stabilize only after the folds creates an inherent separation regime. Moreover, the bistability regime of EPs and WP solutions also depends on the location of the homogeneous Hopf bifurcation (HB), which is a precursor for the organization of EPs around a T-point. In the parameter set chosen here, the HB onset is far from the primary instability onset $s = s_c^t$, so the bistability region is absent. However, we cannot exclude bistability under a different parameter setting. This is left for future explorations. In the case of large mass M (Figures 6 and 19), the LW onset is "enclosed" by the HB balloon (Figure 3), so that the WP solutions also remain unstable after the fold, automatically excluding bistability. Therefore, we believe that bistability between EPs and WP solutions is unlikely to be observed, although we do not definitively exclude this possibility. In the moderate domain size limit (Figure 10), TW and WP solutions show bistability over a broad range of conditions since they are connected through the codimension-2 LW/WB bifurcation, regardless of the criticality of the TWs.

The effect of mass conservation appears more profound than expected [11] (and the references therein), near linear or global bifurcations. For example, the former could relate to bifurcation criticalities and spatial modulations (e.g., see Figure 17) in the unfolding of a codimension-3 bifurcation where LW, WB, and HB instabilities occur simultaneously. This construction should exist based on results shown in Figure 3. Studying global bifurcations could relate to the organizing centers by global T-point bifurcations (as briefly discussed in Section 5 and shown in Figure 7). Note that a detailed study was recently conducted for a multi-variable reaction-diffusion model (albeit without mass conservation) [35]. Other avenues to further study mass-conserved RD systems and their implications for cell behaviours include the exploration of parameter space to acquire elaborated intuition about the initial conditions and perturbations that determine the selection of cell motility modes, especially informative for experimental setups, in the spirit of [30, 49, 67] or the study of interactions leading to cell deformations, as inspired by [15, 16, 19, 21, 40, 44, 52, 55, 56]. Such interactions between domain geometry and reaction-diffusion dynamics promises to add new challenges and insights.

Consequently, the incorporation of mass conservation not only admits distinct and non-trivial pattern formation characteristics in RD systems due to the steady solutions emerging from the long wavelength bifurcation but also affects the actin dynamics. From Figure 1, we can draw an analogy between the solutions and the cell motility modes: the WP solutions represent polarization, the single wavelength TWs correspond to cell turning, and TWs with two or more wavelengths reflect a ruffling-like state, cf. [1, 19, 26, 64]. Increasing the space dimension and/or structural deformations due to mechanical or stochastic effects, may also lead to disordered motility [16, 22, 29, 38, 39, 41, 43, 44, 59]. This study is, therefore, only the tip of the iceberg, which we hope will stimulate further investigations.

Appendix A. Numerical methods.

A.1. Continuation and stability of steady-state solutions obtained in AUTO.
The travelling waves (TWs), excitable pulses (EPs), travelling fronts (TFs), and wave-pinning (WP) solutions discussed in this work are all solutions to the steady-state problem in co-moving coordinates:

$$
\begin{aligned}
0 &= (b + \gamma u^2)v - (1 + sF + u^2)u + \frac{D}{L^2}\frac{\partial^2 u}{\partial \widetilde{\xi}^2} + \frac{c}{L}\frac{\partial u}{\partial \widetilde{\xi}} && \widetilde{\xi} \in (0,1), \\
0 &= -(b + \gamma u^2)v + (1 + sF + u^2)u + \frac{1}{L^2}\frac{\partial^2 v}{\partial \widetilde{\xi}^2} + \frac{c}{L}\frac{\partial v}{\partial \widetilde{\xi}} && \widetilde{\xi} \in (0,1), \\
0 &= \theta(p_0 + p_1 u - F) + \frac{D_F}{L^2}\frac{\partial^2 F}{\partial \widetilde{\xi}^2} + \frac{c}{L}\frac{\partial F}{\partial \widetilde{\xi}} && \widetilde{\xi} \in (0,1),
\end{aligned}
$$

(A.1)

with periodic boundary conditions (or Neumann for TFs), where $\widetilde{\xi} = (x - ct)/L$ is the normalized TW coordinate. For notational convenience, we drop the tilde. A solution to (A.1) is a TW if $c \neq 0$ and a stationary solution otherwise. Since (2.3) has mass conservation, multiple steady-state solutions to (A.1) exist for a given set of model parameters with distinct average densities. Therefore, we need to include the mass constraint

$$
M = \int_0^1 [u(\xi) + v(\xi)]\,\mathrm{d}\xi,
$$

(A.2)

to pin down the mass of the (u, v)-subsystem. Furthermore, the system is translationally invariant due to no explicit dependence on the spatial variable and the periodic boundary conditions (or the travelling fronts with homogeneous Neumann boundary conditions as these solutions decay rapidly at each boundary). To pin down a specific solution, we follow the usual convention [13, 20] by imposing the phase condition

$$
\int_0^1 (Q(\xi) - \tilde{Q}(\xi))^T \tilde{Q}_\xi(\xi)\,\mathrm{d}\xi = 0,
$$

(A.3)

where $Q = (u, v, F)^T$ is the current solution and $\tilde{Q}$ is the previous solution computed on the branch. Intuitively, this condition can be thought to keep a steep front or peak at the same location [13].

Continuation of all steady-state solutions in this work requires three free parameters, the main bifurcation parameter, and two extra parameters for the integral constraints. For TW solutions, the wave speed c is the common choice for the phase condition. However, there are no obvious choices for the mass constraint and the phase condition with stationary patterns. Therefore, we add two additional "dummy" parameters, κ and ψ, into our system. The integral constraints force these quantities to be small. The new steady-state problem is

$$0 = (b + \gamma u^2)v - (1 + sF + u^2)u + \kappa + \frac{D}{L^2}\frac{\partial^2 u}{\partial \xi^2} + \frac{c}{L}\frac{\partial u}{\partial \xi} \quad \xi \in (0,1),$$

(A.4)
$$0 = -(b + \gamma u^2)v + (1 + sF + u^2)u + \frac{1}{L^2}\frac{\partial^2 v}{\partial \xi^2} + \frac{c + \psi}{L}\frac{\partial v}{\partial \xi} \quad \xi \in (0,1),$$

$$0 = \theta(p_0 + p_1 u - F) + \frac{D_F}{L^2}\frac{\partial^2 F}{\partial \xi^2} + \frac{c}{L}\frac{\partial F}{\partial \xi} \quad\quad\quad\quad \xi \in (0,1).$$

The dummy parameter κ perturbs the equation for u. The mass constraint (A.2) ensures that κ is small. Whereas ψ perturbs the wave speed c in the v equation and is forced small by the lack of first derivative terms in the u and F equations, when $c = 0$. The continuation of stationary solutions uses the free parameters $\{s, \kappa, \psi\}$ and the continuation of propagating solutions uses the free parameters $\{s, c, \kappa\}$. In our bifurcation plots, $\kappa, \psi < 10^{-12}$.

To compute the stability of a solution, we use linear stability analysis. We first construct the linear eigenproblem. Retaining the time derivative in the TW problem (A.1) gives

(A.5a)
$$\frac{\partial u}{\partial t} = \frac{D}{L^2}\frac{\partial^2 u}{\partial \xi^2} + \frac{c}{L}\frac{\partial u}{\partial \xi} + \gamma u^2 v - (1 + sF + u^2)u,$$

(A.5b)
$$\frac{\partial v}{\partial t} = \frac{1}{L^2}\frac{\partial^2 v}{\partial \xi^2} + \frac{c}{L}\frac{\partial v}{\partial \xi} + (1 + sF + u^2)u - \gamma u^2 v,$$

(A.5c)
$$\frac{\partial F}{\partial t} = \frac{D_F}{L^2}\frac{\partial^2 F}{\partial \xi^2} + \frac{c}{L}\frac{\partial F}{\partial \xi} + \theta(p_0 + p_1 u - F),$$

on $\xi \in (0,1)$. To determine the stability of a steady state solution $Q_{SS}(\xi)$ to (A.5) we investigate perturbations of the form

(A.6)
$$Q(\xi, t) = Q_{SS}(\xi) + \epsilon \widetilde{Q}(\xi)e^{\mu t},$$

where $|\epsilon| \ll 1$ and $\widetilde{Q}$ is $\mathcal{O}(1)$. Linearization leads to an eigenvalue problem

(A.7)
$$\mathscr{L}\widetilde{Q} := \mathbb{D}\widetilde{Q}'' + c\widetilde{Q}' + \mathcal{L}(Q_{SS}(\xi))y = \mu\widetilde{Q}$$

with the same boundary conditions, where $\widetilde{Q} = (\widetilde{u}, \widetilde{v}, \widetilde{F})^T$ denotes the usual components of the model and $\mathbb{D} = \text{diag}(D/L^2, 1/L^2, D_F/L^2)$ is a diagonal matrix of the scaled diffusion coefficients. A solution is linearly stable if all $Re(\mu) < 0$ and unstable otherwise. We use second-order centred finite difference approximations for the derivatives to approximate the eigenvalues of this infinite-dimensional linear operator $\mathscr{L}$. The solutions from AUTO are converted onto a uniform grid using a built-in splining function in Matlab, *spline*. For computational efficiency, we compute a subset of the eigenvalues near the origin using the built-in

Matlab function *eigs*. This process requires some tuning for each branch as some solutions require many eigenvalues (≈ 30) to ensure the largest real-part eigenvalue is found. Special care must also be taken as both the mass and phase conditions imply zero eigenvalues with linearly independent eigenfunctions. Due to the discretization errors and the errors from the eigenvalue solver, these zero eigenvalues can become quite large, on the order of 10^{-4}. Therefore, to identify bifurcation points we plot the eigenvalues and identify crossings of the imaginary axis. Stability is then verified using time-dependent simulations (see Appendix A.3 for the implementation of time-dependent simulations).

A.2. Continuation and stability of standing wave solutions obtained in AUTO. Standing wave (SW) solutions are time-periodic solutions to the full PDE system (2.3) and are thus two-dimensional (space and time). Hence, one dimension must be discretized as AUTO only deals with one-dimensional boundary value problems. We discretized (2.3) in space using the same centred finite difference scheme discussed in Appendix A.1, leaving us with a large system of $3n$ ODEs, where n is the number of discrete points.

As with the steady-state boundary value problem (BVP), we need to include the mass constraint. Integral constraints in AUTO can only be applied with respect to the independent variable, in this case, time. Since the mass is conserved through time we can control the average mass; thus, fixing it at each time point. The integral constraint is thus

$$(A.8) \qquad M = \frac{1}{TL} \int_0^T \int_0^L [u(x,t) + v(x,t)] \mathrm{d}x \mathrm{d}t,$$

where T is the temporal period. Using our spatial discretization, we can write out the AUTO implementation as

$$(A.9) \qquad 0 = \int_0^1 \Delta x \sum_{i=1}^n [u_i(t) + v_i(t)] \mathrm{d}t - M,$$

where Δx is the spatial discretization width and the time domain has been scaled to $[0, 1]$. We include the same phase condition above but in time to address the translational invariance [13]. Lastly, we use the boundary value problem type in AUTO that also performs Floquet multiplier calculations; thus, computing the stability at each step [20].

A.3. Time-dependent simulation methods. Time-dependent simulations were performed in Julia using a Method of Lines approach [53]. The spatial domain was discretized using the same second-order centred finite differencing used in the stability analysis (see Appendix A.1). The resulting large system of ODEs was integrated using the *Rodas*4P method from the Julia DifferentialEquations package [48], which is a Rosenbrock method purpose-built for semi-discretized non-linear parabolic PDEs [51].

In Figure 18a-d, we show sample profiles of wave-pinning (WP) and travelling wave (TW) solutions used in time-dependent simulations (see Section 6) showcasing the differences in each component. One wavelength of the TW is used to better distinguish between the differences in solution components. As expected, the solution components are qualitatively similar and all non-negative. In Figure 18e,f, we show the real and the imaginary parts of $\widetilde{F}$ that are
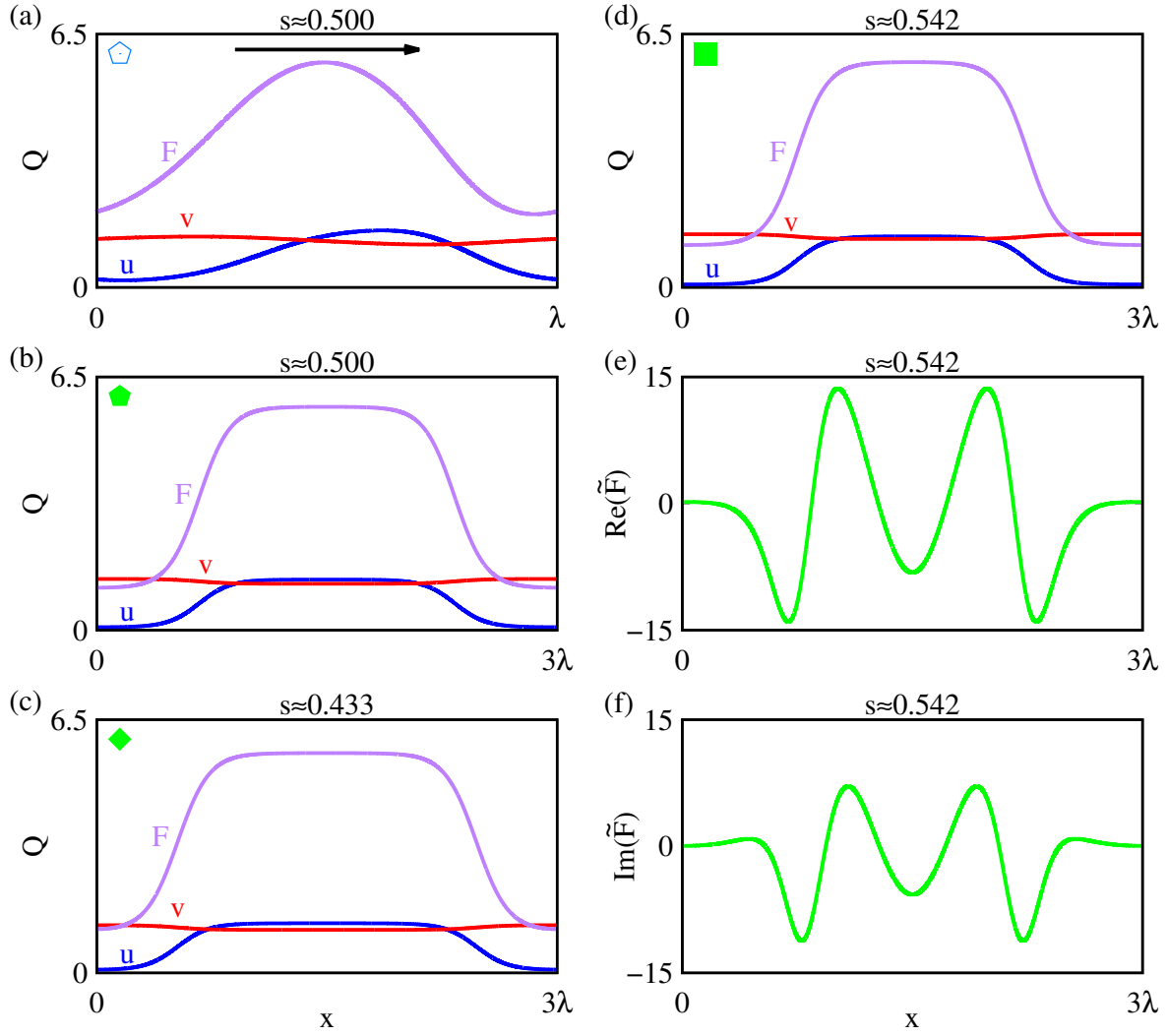
Figure 18: Solution profiles at selected locations in Figure 13 showing all solution components for (a) travelling wave (TW) and (b-d) wave-pinning (WP) solutions on periodic domains; the arrow in (a) denotes the direction of the wave. (e) Real and (f) imaginary parts of the F-component of the leading eigenfunction ($\widetilde{F}$) past the Hopf instability of the $WP_{3\lambda}$ branch at $s \approx 0.554$ (see Figure 13), i.e., instability of the WP solution shown in (c). The critical complex conjugated eigenvalues at the onset are $\mu \approx \pm 0.648i$. The parameter values are given in Table 1 with $M = 2$ and $b = b_c \approx 0.067$.

associated with the critical eigenfunction $\widetilde{Q}$ of a Hopf instability of the $WP_{3\lambda}$ branch at $s \approx 0.554$, for details see Appendix A.1.

Appendix B. Bifurcation structure for the ventral actin wave model.   Yochelis *et*
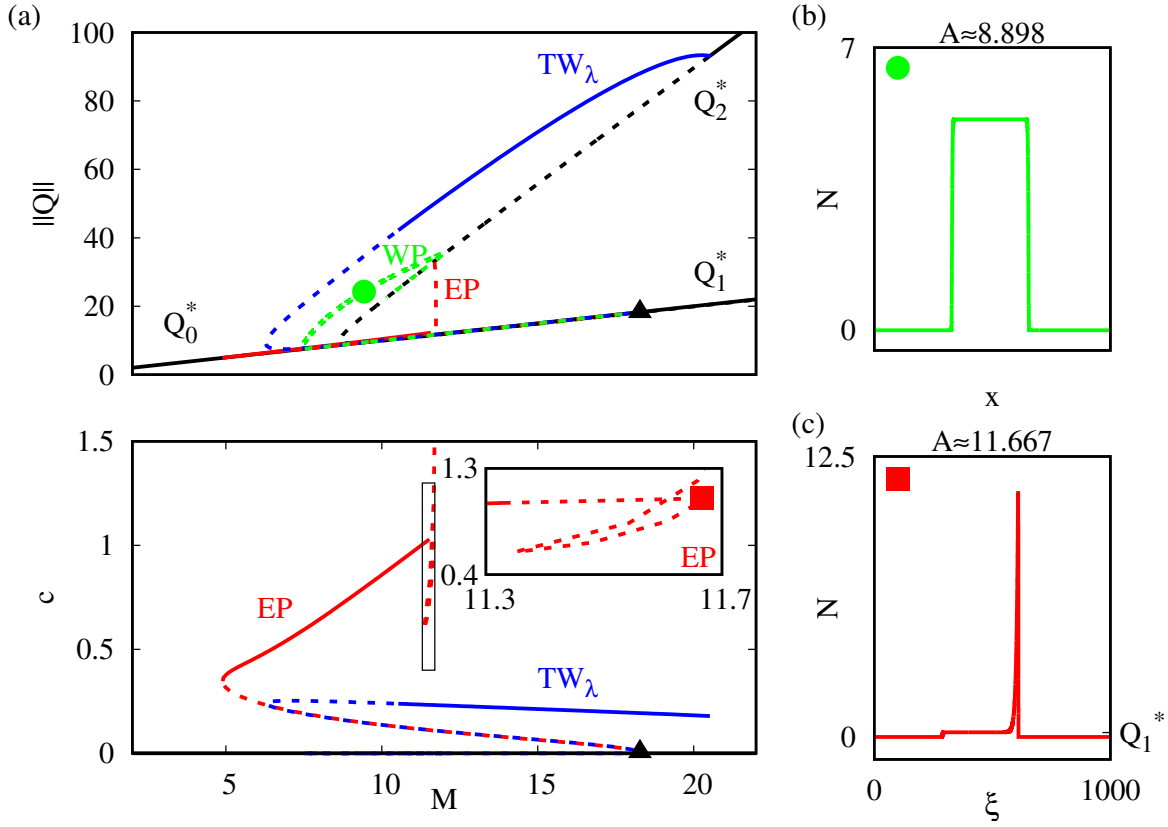
Figure 19: Bifurcation diagrams of (B.1) with respect to total mass M, showing the homogeneous steady states $Q^*_{0,1,2}$, travelling waves (TWs) with critical wavelength λ (TW_λ), wave-pinning (WP) solutions, and excitable pulses (EPs) for $L = 1000 \gg \lambda \approx 4.02$. The solution branches are projected with the Sobolev norm (5.1) and the propagation speed; solid (dashed) lines denote linearly stable (unstable) solutions. The inset in (a) shows the T-point bifurcation (square). In this setting, excitable pulses coexist with travelling waves while the wave-pinning solutions are all unstable. (b,c) Solutions showing a wave-pinning solution (circle) in (b) and a double front solution (square) at the T-point bifurcation (a heteroclinic cycle) in (c). Parameter values: $D_N = 0.1$, $D_I = 0.001$, $r_N = 2$, and $r_I = 0.3$.

al. [66] considered a model describing actin dynamics on the ventral side of cells, comprising F-actin N, G-actin S, and an inhibitor I affecting N,

(B.1)
$$\frac{\partial N}{\partial t} = \frac{N^2 S}{I + 1} - N + D_N \frac{\partial^2 N}{\partial x^2},$$
$$\frac{\partial S}{\partial t} = -\frac{N^2 S}{I + 1} + N + \frac{\partial^2 S}{\partial x^2},$$
$$\frac{\partial I}{\partial t} = r_N N - r_I I + D_I \frac{\partial^2 I}{\partial x^2}.$$

so that the total amount of actin is conserved,

$$(B.2) \qquad M := \frac{1}{L} \int_0^L [N(x,t) + S(x,t)] \mathrm{d}x = \text{constant}.$$

Model details are given in [66], where the F-actin and the G-actin correspond to our active and inactive GTPase and the inhibitor to F-actin. The main difference is that the inhibitor I (our F-actin) does not promote depolymerization (inactivation of the GTPase) but instead inhibits polymerization of actin (activation of the GTPase).

Figure 19 shows the bifurcation structure and properties of travelling waves (TWs), excitable pulses (EPs), and wave-pinning (WP) solutions, along with the homogeneous steady states. (Note that wave-pinning solutions were not investigated in [66]). In this setting, EPs and TWs form a bistability region while the stationary patterns are all unstable - a similar situation in the current study for $M = 4.5$.

REFERENCES

[1] J. ALGORTA, A. FELE-PARANJ, J. M. HUGHES, AND L. EDELSTEIN-KESHET, *Modeling and simulating single and collective cell motility*, Cold Spring Harb. Perspect., to appear.

[2] J. ALLARD AND A. MOGILNER, *Traveling waves in actin dynamics and cell motility*, Curr. Opin. Cell Biol., 25 (2013), pp. 107–115.

[3] Y. ARAI, T. SHIBATA, S. MATSUOKA, M. J. SATO, T. YANAGIDA, AND M. UEDA, *Self-organization of the phosphatidylinositol lipids signaling system for random cell migration*, Proc. Natl. Acad. Sci., 107 (2010), pp. 12399–12404.

[4] M. A. AVILA PONCE DE LEÓN, B. FÉLIX, AND H. G. OTHMER, *A phosphoinositide-based model of actin waves in frustrated phagocytosis*, J. Theoret. Biol., 527 (2021), 110764.

[5] A. BAILLES, E. W. GEHRELS, AND T. LECUIT, *Mechanochemical principles of spatial and temporal patterns in cells and tissues*, Annu. Rev. Cell Dev. Biol., 38 (2022), pp. 321–347.

[6] E. L. BARNHART, J. ALLARD, S. S. LOU, J. A. THERIOT, AND A. MOGILNER, *Adhesion-dependent wave generation in crawling cells*, Curr. Biol., 27 (2017), pp. 27–38.

[7] W. M. BEMENT, A. B. GORYACHEV, A. L. MILLER, AND G. VON DASSOW, *Patterning of the cell cortex by Rho GTPases*, Nat. Rev. Mol. Cell Biol., 25 (2024), pp. 290–308.

[8] W. M. BEMENT, M. LEDA, A. M. MOE, A. M. KITA, M. E. LARSON, A. E. GOLDING, C. PFEUTI, K.-C. SU, A. L. MILLER, A. B. GORYACHEV, AND G. VON DASSOW, *Activator–inhibitor coupling between Rho signalling and actin assembly makes the cell cortex an excitable medium*, Nat. Cell Biol., 17 (2015), pp. 1471–1483.

[9] E. BERNITT, H.-G. DÖBEREINER, N. S. GOV, AND A. YOCHELIS, *Fronts and waves of actin polymerization in a bistability-based mechanism of circular dorsal ruffles*, Nat. Commun., 8 (2017), 15863.

[10] C. BETA, L. EDELSTEIN-KESHET, N. GOV, AND A. YOCHELIS, *From actin waves to mechanism and back: How theory aids biological understanding*, eLife, 12 (2023), e87181.

[11] C. BETA, N. S. GOV, AND A. YOCHELIS, *Why a large–scale mode can be essential for understanding intracellular actin waves*, Cells, 9 (2020), 1533.

[12] C. BETA AND K. KRUSE, *Intracellular oscillations and waves*, Annu. Rev. Condens. Matter Phys., 8 (2017), pp. 239–264.

[13] W.-J. BEYN AND V. THÜMMLER, *Phase conditions, symmetries and pde continuation*, in Numerical Continuation Methods for Dynamical Systems: Path following and boundary value problems, B. Krauskopf, H. M. Osinga, and J. Galán-Vioque, eds., Springer Netherlands, Dordrecht, 2007, pp. 301–330.

[14] F. BRAUNS, J. HALATEK, AND E. FREY, *Phase-space geometry of mass-conserving reaction-diffusion dynamics*, Phys. Rev. X., 10 (2020), 041036.

[15] B. A. Camley, Y. Zhao, B. Li, H. Levine, and W.-J. Rappel, *Crawling and turning in a minimal reaction-diffusion cell motility model: coupling cell shape and biochemistry*, Phys. Rev. E, 95 (2017), 012401.

[16] Y. Cao, E. Ghabache, and W.-J. Rappel, *Plasticity of cell migration resulting from mechanochemical coupling*, eLife, 8 (2019), e48478.

[17] A. R. Champneys, F. Al Saadi, V. F. Breña-Medina, V. A. Grieneisen, A. F. Marée, N. Verschueren, and B. Wuyts, *Bistability, wave pinning and localisation in natural reaction–diffusion systems*, Phys D, 416 (2021), 132735.

[18] M. C. Cross and P. C. Hohenberg, *Pattern formation outside of equilibrium*, Rev. Modern Phys., 65 (1993), pp. 851–1123.

[19] H.-G. Döbereiner, B. J. Dubin-Thaler, J. M. Hofman, H. S. Xenias, T. N. Sims, G. Giannone, M. L. Dustin, C. H. Wiggins, and M. P. Sheetz, *Lateral membrane waves constitute a universal dynamic pattern of motile cells*, Phys. Rev. Lett., 97 (2006), 038102.

[20] E. J. Doedel, A. R. Champneys, T. Fairgrieve, Y. Kuznetsov, B. Oldeman, R. Paffenroth, B. Sandstede, X. Wang, and C. Zhang, *Auto07p: Continuation and bifurcation software for ordinary differential equations*, 2012.

[21] K. Doubrovinski and K. Kruse, *Cell motility resulting from spontaneous polymerization waves*, Phys. Rev. Lett., 107 (2011), 258103.

[22] A. Dreher, I. S. Aranson, and K. Kruse, *Spiral actin-polymerization waves can generate amoeboidal cell crawling*, New Journal of Physics, 16 (2014), p. 055007.

[23] C. M. Elliott, M. A. Herrero, J. R. King, and J. R. Ockendon, *The mesa problem: Diffusion patterns for $u_t = \nabla \cdot (u^m \nabla u)$ as $m \to +\infty$*, IMA J. Appl. Math., 37 (1986), pp. 147–154.

[24] R. FitzHugh, *Impulses and physiological states in theoretical models of nerve membrane*, Biophys. J., 1 (1961), pp. 445–466.

[25] G. Gerisch, M. Ecke, B. Schroth-Diez, S. Gerwig, U. Engel, L. Maddera, and M. Clarke, *Self-organizing actin waves as planar phagocytic cup structures*, Cell Adh. Migr., 3 (2009), pp. 373–382.

[26] G. Giannone, B. J. Dubin-Thaler, H.-G. Döbereiner, N. Kieffer, A. R. Bresnick, and M. P. Sheetz, *Periodic lamellipodial contractions correlate with rearward actin waves*, Cell, 116 (2004), pp. 431–443.

[27] A. B. Goryachev and M. Leda, *Many roads to symmetry breaking: molecular mechanisms and theoretical models of yeast cell polarity*, Mol. Biol. Cell., 28 (2017), pp. 370–380.

[28] A. B. Goryachev, M. Leda, A. L. Miller, G. von Dassow, and W. M. Bement, *How to make a static cytokinetic furrow out of traveling excitable waves*, Small GTPases, 7 (2016), pp. 65–70.

[29] S. Hladyshau, M. Kho, S. Nie, and D. Tsygankov, *Spatiotemporal development of coexisting wave domains of rho activity in the cell cortex*, Scientific Reports, 11 (2021), p. 19512.

[30] W. R. Holmes, A. E. Carlsson, and L. Edelstein-Keshet, *Regimes of wave type patterning driven by refractory actin feedback: transition from static polarization to dynamic wave behaviour*, Phys. Biol., 9 (2012), 046005.

[31] W. R. Holmes, J. Park, A. Levchenko, and L. Edelstein-Keshet, *A mathematical model coupling polarity signaling to cell adhesion explains diverse cell migration patterns*, PLoS Comput. Biol., 13 (2017), e1005524.

[32] N. Inagaki and H. Katsuno, *Actin waves: origin of cell polarization and migration?*, Trends Cell Biol., 27 (2017), pp. 515–526.

[33] A. Jilkine and L. Edelstein-Keshet, *A comparison of mathematical models for polarization of single eukaryotic cells in response to guided cues*, PLoS Comput. Biol., 7 (2011), e1001121.

[34] E. Knobloch, *Oscillatory convection in binary mixtures*, Phys. Rev. A, 34 (1986), 1538.

[35] E. Knobloch and A. Yochelis, *Front propagation and global bifurcations in a multivariable reaction-diffusion model*, Chaos, 33 (2023), 053115.

[36] T. Kolokolnikov, T. Erneux, and J. Wei, *Mesa-type patterns in the one-dimensional brusselator and their stability*, Phys. D, 214 (2006), pp. 63–77.

[37] J. Landino, M. Leda, A. Michaud, Z. T. Swider, M. Prom, C. M. Field, W. M. Bement, A. G. Vecchiarelli, A. B. Goryachev, and A. L. Miller, *Rho and F-actin self-organize within an artificial cell cortex*, Curr. Biol., 31 (2021), pp. 5613–5621.

[38] Y. Liu, E. G. Rens, and L. Edelstein-Keshet, *Spots, stripes, and spiral waves in models for static and motile cells*, Journal of Mathematical Biology, 82 (2021), pp. 1–38.

[39] M. Machacek and G. Danuser, *Morphodynamic profiling of protrusion phenotypes*, Biophysical journal, 90 (2006), pp. 1439–1452.

[40] A. F. Marée, V. A. Grieneisen, and L. Edelstein-Keshet, *How cells integrate complex stimuli: the effect of feedback from phosphoinositides and cell shape on cell polarization and motility*, PLoS Comput. Biol., 8 (2012), e1002402.

[41] A. Michaud, M. Leda, Z. T. Swider, S. Kim, J. He, J. Landino, J. R. Valley, J. Huisken, A. B. Goryachev, G. von Dassow, et al., *A versatile cortical pattern-forming circuit based on Rho, F-actin, Ect2 and RGA-3/4*, J. Cell Biol., 221 (2022), e202203017.

[42] A. Michaud, Z. T. Swider, J. Landino, M. Leda, A. L. Miller, G. von Dassow, A. B. Goryachev, and W. M. Bement, *Cortical excitability and cell division*, Curr. Biol., 31 (2021), pp. R553–R559.

[43] T. Moldenhawer, E. Moreno, D. Schindler, S. Flemming, M. Holschneider, W. Huisinga, S. Alonso, and C. Beta, *Spontaneous transitions between amoeboid and keratocyte-like modes of migration*, Frontiers in Cell and Developmental Biology, 10 (2022), p. 898351.

[44] E. Moreno, S. Flemming, F. Font, M. Holschneider, C. Beta, and S. Alonso, *Modeling cell crawling strategies with a bistable model: From amoeboid to fan-shaped cell motion*, Phys. D, 412 (2020), 132591.

[45] Y. Mori, A. Jilkine, and L. Edelstein-Keshet, *Wave-pinning and cell polarity from a bistable reaction-diffusion system*, Biophys. J., 94 (2008), pp. 3684–3697.

[46] Y. Mori, A. Jilkine, and L. Edelstein-Keshet, *Asymptotic and bifurcation analysis of wave-pinning in a reaction-diffusion model for cell polarization*, SIAM J. Appl. Math., 71 (2011), pp. 1401–1427.

[47] J. Nagumo, S. Arimoto, and S. Yoshizawa, *An active pulse transmission line simulating nerve axon*, Proc. IRE, 50 (1962), pp. 2061–2070.

[48] C. Rackauckas and Q. Nie, *Differentialequations.jl–a performant and feature-rich ecosystem for solving differential equations in Julia*, J. Open Res. Softw., 5 (2017), 15.

[49] E. G. Rens and L. Edelstein-Keshet, *Cellular tango: How extracellular matrix adhesion choreographs rac-rho signaling and cell movement*, Phys. Biol., 18 (2021), 066005.

[50] A. J. Ridley, *Rho GTPase signalling in cell migration*, Curr. Opin. Cell Biol., 36 (2015), pp. 103–112.

[51] G. Steinebach, *Construction of Rosenbrock–Wanner method Rodas5P and numerical benchmarks within the Julia differential equations package*, BIT Numer. Math., 63 (2023), 27.

[52] D. Taniguchi, S. Ishihara, T. Oonuki, M. Honda-Kitahara, K. Kaneko, and S. Sawai, *Phase geometries of two-dimensional excitable waves govern self-organized morphodynamics of amoeboid cells*, Proc. Natl. Acad. Sci., 110 (2013), pp. 5016–5021.

[53] L. N. Trefethen, *Finite difference and spectral methods for ordinary and partial differential equations*, Cornell University Dept. of Computer Science and Center for Applied Mathematics, 1996.

[54] A. M. Turing, *The chemical basis of morphogenesis*, Philos. Trans. R. Soc. B, 237 (1952), pp. 37–72.

[55] B. Vanderlei, J. J. Feng, and L. Edelstein-Keshet, *A computational model of cell polarization and motility coupling mechanics and biochemistry*, Multiscale Model. Simul., 9 (2011), pp. 1420–1443.

[56] F. Veerman, M. Mercker, and A. Marciniak-Czochra, *Beyond turing: Far-from-equilibrium patterns and mechano-chemical feedback*, Philos. Trans. R. Soc. A, 379 (2021), 20200278.

[57] N. Verschueren and A. Champneys, *A model for cell polarization without mass conservation*, SIAM J. Appl. Dyn. Syst., 16 (2017), pp. 1797–1830.

[58] M. G. Vicker, *F-actin assembly in Dictyostelium cell locomotion and shape oscillations propagates as a self-organized reaction–diffusion wave*, FEBS Lett., 510 (2002), pp. 5–9.

[59] O. D. Weiner, W. A. Marganski, L. F. Wu, S. J. Altschuler, and M. W. Kirschner, *An actin-based wave generator organizes cell motility*, PLoS Biology, 5 (2007), p. e221.

[60] O. D. Weiner, G. Servant, M. D. Welch, T. J. Mitchison, J. W. Sedat, and H. R. Bourne, *Spatial control of actin polymerization during neutrophil chemotaxis*, Nat. Cell Biol., 1 (1999), pp. 75–81.

[61] K. Wong, O. Pertz, K. Hahn, and H. Bourne, *Neutrophil polarization: Spatiotemporal dynamics of RhoA activity support a self-organizing mechanism*, Proc. Natl. Acad. Sci., 103 (2006), pp. 3639–3644.

[62] M. Wu, X. Wu, and P. De Camilli, *Calcium oscillations-coupled conversion of actin travelling waves to standing oscillations*, Proc. Natl. Acad. Sci., 110 (2013), pp. 1339–1344.

[63] F. Xiao, J. Li, K. Huang, X. Li, Y. Xiong, M. Wu, L. Wu, W. Kuang, S. Lv, L. Wu, et al., *Macropinocytosis: mechanism and targeted therapy in cancers*, Am. J. Cancer Res., 11 (2021), pp. 14–30.

[64] T. D. Yang, K. Park, J.-S. Park, J.-H. Lee, E. Choi, J. Lee, W. Choi, Y. Choi, and K. J. Lee, *Two distinct actin waves correlated with turns-and-runs of crawling microglia*, PloS One, 14 (2019), e0220810.

[65] Y. Yang and M. Wu, *Rhythmicity and waves in the cortex of single cells*, Philos. Trans. R. Soc. B, 373 (2018), 20170116.

[66] A. Yochelis, S. Flemming, and C. Beta, *Versatile patterns in the actin cortex of motile cells: Self-organized pulses can coexist with macropinocytic ring-shaped waves*, Phys. Rev. Lett., 129 (2022), 088101.

[67] C. Zmurchok and W. R. Holmes, *Simple Rho GTPase dynamics generate a complex regulatory landscape associated with cell shape*, Biophys. J., 118 (2020), pp. 1438–1454.